PHYSIK–DEPARTMENT

Structural changes in lamellar diblock copolymer thin films during solvent vapor treatment

Dissertation
von
Zhenyu Di

TECHNISCHE UNIVERSITÄT
MÜNCHEN

TECHNISCHE UNIVERSITÄT MÜNCHEN

Lehrstuhl für Funktionelle Materialien
Physik-Department E13

Structural changes in lamellar diblock copolymer thin films during solvent vapor treatment

Zhenyu Di

Vollständiger Abdruck der von der Fakultät für Physik der Technischen Universität München zur Erlangung des akademischen Grades eines

Doktors der Naturwissenschaften (Dr. rer. nat.)

genehmigten Dissertation.

Vorsitzender: Univ.-Prof. Dr. Ralf Metzler

Prüfer der Dissertation:
1. Univ.-Prof. Dr. Christine Papadakis
2. Univ.-Prof. Dr. Katharina Krischer

Die Dissertation wurde am 30.03.2010 bei der Technischen Universität München eingereicht und durch die Fakultät für Physik am 27.04.2010 angenommen.

Abstract

This research work focuses on the structural changes in thin films of lamellar poly(styrene-*b*-butadiene) diblock copolymer during solvent vapor treatment. Two kinds of solvent were used in this work: cyclohexane and cyclohexanone. The cyclohexane is slightly polybutadiene selective while cyclohexanone is slightly polystyrene selective. Two vapor treatments were carried out using cyclohexane: one was in saturated vapor atmosphere and the other was under stepwise-increasing vapor pressure. For cyclohexanone, since its saturated vapor pressure is very low already, only the vapor treatment in saturated vapor atmosphere was carried out.

To study the film inner structural changes during vapor treatment, in situ grazing-incidence small angle X-ray scattering (GISAXS) measurements were performed. The GISAXS offered a time resolution up to a few seconds thus the fast structural changes was well followed. With the help of GISAXS measurements, the lamellae and film swelling, the improvement of the long-range order and the phase transition were observed. We attribute the observations to the change of the glass transition temperature, the Flory-Huggins segment-segment interaction parameter and/or the volume fraction of one block.

Contents

1 Introduction **1**

1.1 Block copolymer thin films 1

1.2 Vapor treatment 3

2 Strategy of this work **5**

3 Theory of block copolymer solvent blends **7**

3.1 Flory-Huggins segment-segment interaction parameter 7

3.1.1 Dry sample 7

3.1.2 Polymer-solvent blend 10

3.2 Concentration dependence of T_g 11

3.2.1 T_g of the polymer 11

3.2.2 T_g of the solvent 11

3.2.3 T_g of the polymer-solvent blend 12

3.3 Selectivity of solvent 13

4 Experimental **17**

4.1 The samples 17

4.2 White light interferometer 18

4.2.1 Methods 18

4.2.2 Setup 18

4.2.3 Data analysis 19

4.3 X-ray reflectivity 20

4.3.1 Methods 20

4.3.2 Setup 20

4.3.3 Data analysis 21

4.4 GISAXS 21

4.4.1 Methods 21

4.4.2 Setup 22

4.4.3 Data analysis 24
4.4.3.1 Lamellar orientation 24
4.4.3.2 Two banches of scattering 24
4.4.3.3 Fitting of the DBSs 25
4.4.3.4 Scattering depth 26

5 Vapor treatment with saturated CHX 27
5.1 Idea 27
5.2 Experimental 27
5.3 Results 28
5.3.1 Structure of the as-prepared film 28
5.3.1.1 X-ray reflectivity 28
5.3.1.2 GISAXS 29
5.3.2 Structure changes during vapor treatment 33
5.3.2.1 Lamellar thickness 35
5.3.2.2 Film thickness 36
5.3.2.3 Domain size 37
5.3.3 Maximum film swelling 37
5.4 Discussion 38
5.4.1 Decrease of the effective T_g 39
5.4.2 Decrease of χ_{eff} 39
5.4.3 Increase of the degree of coiling 40
5.4.4 Behavior of randomly oriented lamellae 42
5.5 Conclusion 42

6 Stepwise vapor treatment with CHX 45
6.1 Idea 45
6.2 Experimental 45
6.3 Results and discussion
6.3.1 Structure of the as-prepared film 47

6.3.2 The first step of swelling 49
6.3.2.1 Stable state 50
6.3.2.2 The transition process 52
6.3.2.3 Lamellae swelling 53
6.3.3 Further swelling 56
6.3.3.1 Nonequilibrium 56
6.3.3.1.1 Results 56
6.3.3.1.2 Discussion 57
6.3.3.2 Scalling law 58
6.4 Conclusion 59
6.4.1 The first swelling-step 59
6.4.2 The other swelling-steps 60

7 Vapor treatment with saturated CHXO 63

7.1 Idea 63
7.2 Setup 63
7.3 Results and discussion 64
7.3.1 Structure of the as-prepared film 64
7.3.2 Structural changes in saturated CHXO 66
7.3.2.1 Long-range order 67
7.3.2.2 Lamellar thickness 68
7.3.2.3 Side maximum 68
7.3.2.4 Elongation and bending of DBSs 70
7.3.2.5 Dewetting of the thin film 70
7.4 Conclusion 70
7.4.1 Fast process 71
7.4.2 Slow process 71

8 Summary 73

Chapter 1

Introduction

1.1 Block copolymer thin films

Block copolymers are macromolecules containing different species of monomers, which are arranged in blocks. The monomers constituting the blocks (*A* and *B*) are in most cases immiscible, thus a decrease in *A-B* segment-segment contacts reduces the system enthalpy *H,* which motivates the micro-phase separation. However, the micro-phase separation decreases the entropy. Therefore, the immiscibility of the different block must be big enough so that the enthalpic factors can dominate the entropic factors. Thanks to Flory [1] and Huggins [2], the immiscibility of the two blocks can be expressed by the product of χN, where χ is Flory-Huggins segment-segment interaction parameter and *N* is the overall degree of polymerization. When $\chi N > 0$, the two blocks are immiscible but only when $\chi N > (\chi N)_{ODT}$, where ODT represents order-to-disorder transition, the enthalpic factors can dominate the entropic factors and the micro-phase separation is possible. Depending on χN and the volume fraction of one block, f_A, the block copolymer shows various micro-phase behaviors as lamellae, gyroid, cylinders or spheres (Figure 1.1).

Because of the ability to self-assemble into a rich variety of periodic patterns, which have repeat distances typically in the range of 10 to 100 nm [3, 4], block copolymer thin films have the potential for a number of nanotechnology applications. For example, Thurn-Albrecht et al. used poly(styrene-*b*-methylmethacry) thin films to produce the templates for nano-wire arrays [5]. In their system the volume fraction of styrene is 0.71, so that the copolymer self-assembles into arrays of PMMA cylinders hexagonally packed in a PS matrix (Figure 1.2 A). Deep ultraviolet exposure was performed afterwards to degrade the PMMA domains and simultaneously cross-link the PS matrix such that the degraded PMMA can be removed by rinsing with acetic acid (Figure 1.2 B). Electro-deposition is used to fill the nanopores with continuous metal nano-wires (Figure 1.2 C). The nano-wire has a density in excess of 1.9×10^{11} wires per square centimeter that point toward a route to ultrahigh-density storage media. Urbas et al. used poly(styrene-*b*-isoprene) symmetric diblock copolymer-homopolymer blends as one-

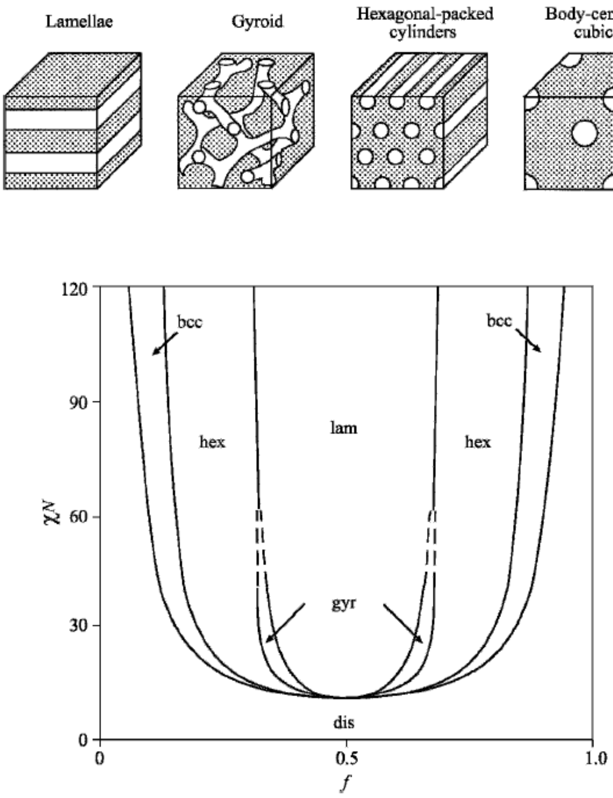

Figure 1.1 Phase diagram for diblock copolymer calculated using self-consistent mean field theory [6, 7]. In the phase diagram, regions of stability of disordered (dis), lamellar (lam), gyroid (gyr), hexagonal (hex) and body-centred cubic (bcc) phases are indicated.

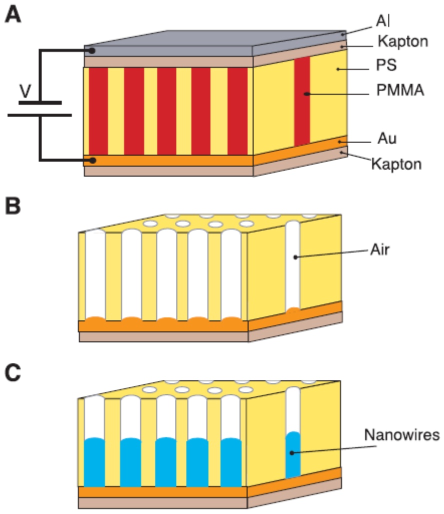

Figure 1.2 A schematic representation of high-density nanowire fabrication in a polymer matrix. (A) An asymmetric diblock copolymer annealed above the glass transition temperature of the copolymer between two electrodes under an applied electric field, forming a hexagonal array of cylinders oriented normal to the film surface. (B) After removal of the minor component, a nanoporous film is formed. (C) By electrodeposition, nanowires can be grown in the porous template, forming an array of nanowires in a polymer matrix. Figure taken from [5].

dimensionally periodic dielectric reflectors [8]. They cast-coated a 0.5 mm thin film from blend of P(S-*b*-I) and homopolyisoprene. Polystyrene and polyisoprene self-assembled into lamellae parallel to the film surface with a lamellar thickness of 130 nm. Thus only the light with a wave length around 450 nm can be efficiently reflected. More examples of the applications of block copolymer thin film can be listed e.g. molecular sieves [9], and sensors [10], solar cells [11] …

1.2 Vapor treatment

In many applications, there is a common requirement: long-range order of the nano-structure. However, self-assembly doesn´t necessarily lead to long-range order. Only when the repulsion between the different blocks is big enough and the block copolymer is in micro-phase equilibrium, the long-range ordered micro-phase separation can be achieved. The former condition can be fulfilled by choosing the block copolymer system properly. The latter is achieved by thermal annealing or vapor treatment.

Thermal annealing is the most commonly used method, because it is straightforward and efficient in many cases. By heating the block copolymer above the glass transition temperatures of the blocks, the chain mobility increases, and thermodynamic equilibrium can be achieved [12]. However, this process does not apply to all polymers. Some polymers have a T_g close to their thermal degradation temperature, whereas others crosslink during annealing at high temperature. For example, conductive polymers are normally hard and thus difficult to use thermal annealing to achieve equilibrium.

Treatment with solvent vapor circumvents these problems and therefore attracts increasing interest. Many groups have reported the improvement of long-range order *after* vapor treatment and subsequent drying [13-16]. For instance, Kim et al showed that vapor treatment of a thin film of cylinder-forming poly(styrene-*b*-ethylene oxide) with the common solvent benzene and subsequent drying resulted in highly oriented, nearly-defect-free arrays of cylinders, which spanned the entire film thickness [16]. In in-situ measurements *during* vapor treatment on similar films they found that ion complexation of the PEO block enhances the long-range order upon solvent annealing. They attributed this finding to the increase of the effective segmental interactions χ between PS and PEO by the presence of the salt [17]. Fukunaga et al. carried out vapor treatment of a terblock copolymer thin film using tetrahydrofuran, a common solvent for all three blocks. From Figure 1.3 it is seen that the initial short-range ordered sponge-like morphology before vapor treatment transformed into long-range ordered lamellae, starting near the air-polymer interface, which results in a multilayered structure throughout the film [18]. Albalak et al. studied the structural changes of poly(styrene-*b*-butadiene-*b*-styrene) triblock copolymers after exposure to the vapor of hexane, methylethylketone and toluene, respectively. They observed an improvement of the long-range order and a complex behavior of the repeat distance as a function of vapor treatment time [19].

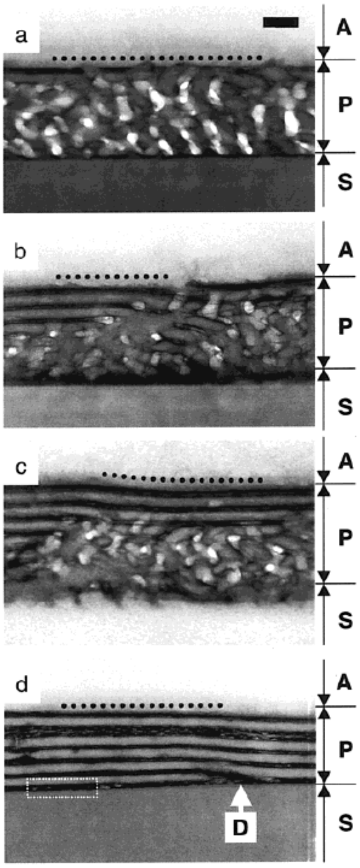

Figure 1.3 Cross-sectional TEM images showing the time evolution of self-assembly in the thin SVT triblock terpolymer film: as-prepared (a), after the THF vapor treatment for 5 s (b, c). and 1 min (d). The black scale bar, common for the all images, in the topmost figure represents 100 nm. The embedding matrix, the substrate, and the triblock terpolymer film are in the portion A, S, and P, respectively. PS, P2VP, and PtBMA microdomains appear bright, dark, and gray, respectively, in the TEM images. Dotted lines represent the approximate position of the free surface in the respective images. In (d), a dislocation core is indicated by *D*. (Figure taken from [18])

However, most of the previous studies only showed that the vapor treatment have the capability to improve the micro-phase separation of the block copolymer thin films. The underlying molecular processes occurring during vapor treatment are still not well understood. For example, it is unclear why the vapor treatment does not improve the long-range order in all systems [17]. It would be desirable to know which conditions – choice of solvent, vapor pressure, duration of treatment time, conditions of drying etc. – are optimum for obtaining the desired structure. Moreover, a detailed understanding of the processes during restructuring is desirable for the optimization.

Chapter 2

Strategy of this work

The goal of this work is to study the mechanism and the underlying molecular processes occurring in thin films of lamellar P(S-*b*-B) block copolymer during vapor treatment. We investigate the influences of the solvent to the micro-phase separation: The phase diagram, the long-range order and the structure dimension.

For this purpose, three in-situ, real-time grazing-incidence small-angle X-ray scattering (GISAXS) experiments were carried out during vapor treatment. In the first two experiments, cyclohexane (CHX) was used as solvent for vapor treatment (Chapter 5, Chapter 6), while in the third experiment, cyclohexanone (CHXO) was used (Chapter 7). The CHX is slightly polybutadiene (PB) selective while the CHXO is slightly polystyrene (PS) selective.

In Chapter 3, the theory of block copolymer-solvent blends will be discussed focusing on the parameters which are most important during vapor treatment i.e the glass transition temperature, T_g, the Flory-Huggins segment-segment interaction parameter, χ and the selectivity of the solvent.

In Chapter 4, the experimental methods and setup are introduced including the sample preparation, white light interferometer, X-ray reflectivity and GISAXS.

In Chapter 5, a block copolymer thin film with initially short-range ordered, randomly oriented lamellae was exposed in saturated solvent vapor atmosphere. Drastic changes of the inner structure were observed: (i) The long-range order of the lamellar micro-phase separation first improved and then became worse and at last the sample became disordered. (ii) The lamellar thickness of the of the parallel lamellae first increased quickly and then decrease slowly and at last leveled off with a value slightly larger than that in the dry state. We related the changes to the influence of the solvent vapor on T_g and χN .

In Chapter 6, the vapor treatment conditions were improved with an additional possibility to adjust the vapor pressure. The block copolymer thin film was exposed to a solvent vapor atmosphere where the vapor pressure increased stepwise. In each vapor pressure/step, the thin film was exposed for enough time until the sample was stable (time independent). Thus the lamellar thickness of the parallel lamellae can be expressed only as a function of the volume fraction of the polymer, ϕ, but independent of time. Moreover, stable states with improved long-range order of the lamellar micro-phase separation were observed in some of the vapor pressure/step.

In Chapter 7 the solvent for vapor treatment was changed from CHX to CHXO. The idea is that: in the block copolymer, the PB is the soft block and PS is the rigid block. Thus the PS selective CHXO could soften the sample better. Furthermore, CHXO has a lower glass transition temperature than that of CHX, which would also benefit the softening. However, since the vapor pressure of CHXO is very low, only vapor treat in saturated CHXO vapor was performed. An improvement of the lamellar micro-phase separation and the transition of micro-phase were observed.

In Chapter 8 a summary and conclusion of this work is drawn.

Chapter 3

Theory of block copolymer-solvent blends

In this chapter, the parameters which are important for understanding the observations in this work will be discussed. Each of them plays a key role during vapor treatment.

3.1 Flory-Huggins segment-segment interaction parameter

3.1.1 Dry sample

In this section, the micro-phase separation of block copolymers will be discussed focused on the Flory-Huggins segment-segment interaction parameter, χ , which is defined by [20]

$$\chi = \frac{1}{k_B T}\left[\varepsilon_{AB} - \frac{1}{2}\left(\varepsilon_{AB} + \varepsilon_{BB}\right)\right] \qquad (3.2)$$

where ε_{ij} denotes the contact energy between i and j segments and k_B the Boltsmann constant. $k_B T \chi$ represents the change in enthalpy when bringing, say, an A-segment from a pure A-environment to a pure B-environment [21]. If χ is negative, mixing is favorable, this may be the case with hydrogen bonding; if χ is positive, the interaction between different segments is repulsive. The physical origin of the interaction between nonpolar monomers, such as the polystyrene or polybutadiene monomers, is the van der Waals interaction, also termed "dispersion forces" [22]. These forces arise from the fluctuating electric field created by the electrons oscillating around the nucleus in an atom, which may polarize nearby atoms. The resulting interaction between two equal atoms can be shown to be attractive [19]. Dispersion forces are at the origin of the crystallization of noble gases, for instance. The total intermolecular pair potential is obtained by adding the long-range attractive van-der-Waals-potential ($\propto 1/r^6$) and the repulsive hard-core potential, which is short-ranged ($\propto 1/r^{12}$). The simple picture valid for small spherical atoms has to be refined for anisotropic molecules, such as polymer segments, which may align each other upon mixing.

To learn the micro-phase behavior, we will start with a simpler case, a polymer blend. The micro-phase behavior of polymer blend can be described by the Flory-Huggins theory. Here we consider a mixture of polymers *A* and *B* with a polymerization index N_A and N_B, respectively. The volume fraction of component *A* in the blend is ϕ. The free energy of mixing is given by

$$\frac{\triangle F_{\mathrm{mix}}}{kT} = \frac{1}{N_A}\phi\ln\phi + \frac{1}{N_B}(1-\phi)\ln(1-\phi) + \chi\phi(1-\phi) \tag{3.1}$$

where *k* is the Boltzmann constant, *T* is the absolute temperature and χ is the Flory-Huggins interaction parameter characterizing the effective interaction of monomers *A* and *B*. Figure 3.1 shows a composition dependence of the free energy of mixing for a symmetric polymer blend ($N_A = N_B = N$) with the product $\chi N = 2.7$ and the corresponding phase diagram. The binodal line corresponds to the micro-phase boundary and for binary mixtures coincides with the coexistence curve. The spinodal line separates the ordered region into the meta-stable region and the unstable region. The lowest point on the spinodal curve corresponds to the critical point ($\phi_c = 1/2$). The spinodal and binodal for any binary mixture meet at the critical point. For χ below the critical one (χ_c) the homogeneous mixture is stable at any composition. For higher values of the χ, there is a miscibility gap between the two branches of the bimodal in Figure 3.1. For any composition in a miscibility gap, the equilibrium state corresponds to two phases with compositions ϕ' and ϕ'' located on the two branches of the coexistence curve at the same value of χ [23].

However, the Flory-Huggins theory can not perfectly describe the micro-phase separation of a block copolymer. In this context, Bates and Fredrickson [3] have given a representative review of the experimental and theoretical developments in block copolymer thermodynamics. In the strong segregation limit, the experimental results show the various micro-phase equilibrium morphologies depending on the volume fraction of the block components. Most of these equilibrium morphologies (spherical, cylindrical and lamellar morphologies) are in close agreement with theoretical predictions [24], based on the self-consistent-field theory proposed by Helfand [25]. In order to investigate the ODT, Leibler [26] constructed a Landau expansion

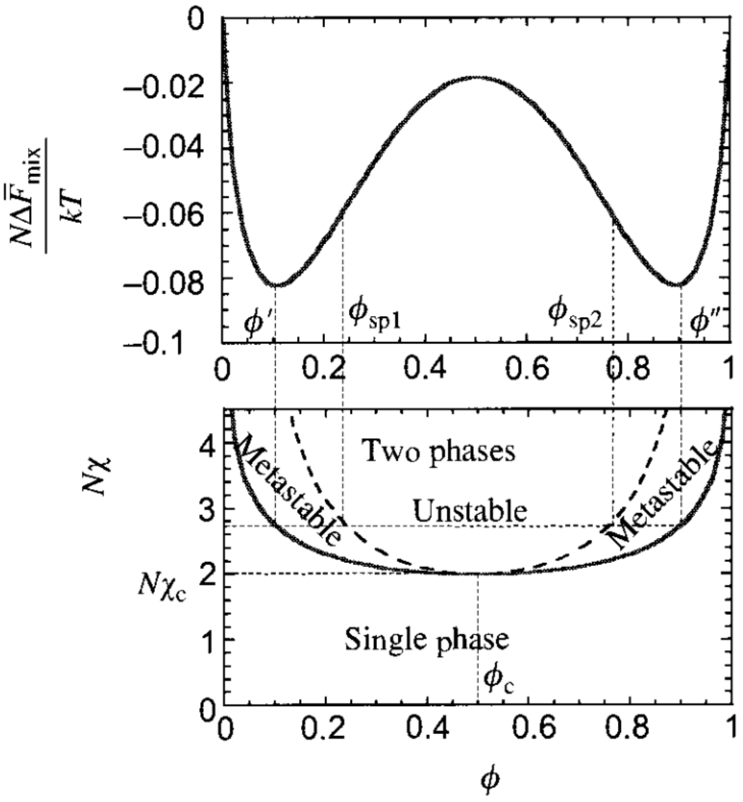

Figure 3.1 Composition dependence of the free energy of mixing for a symmetric polymer blend with the product χN =2.7 (top figure) and the corresponding phase diagram (bottom figure). Binodal (solid curve) and spinodal (dashed curve) are shown on the phase diagram. (Figure taken from [23])

of the free energy to the fourth order of a compositional order parameter. By using a random phase approximation [27], Leibler was able to locate the microphase separation transition (MST), at which a homogeneous block copolymer melt first orders. For the sake of simplicity, he considered an *A*-*B* diblock copolymer with all the chains having the same index of polymerization $N = N_A + N_B$ (N_A and N_B denote the number of monomers of type A and B, respectively) and the same composition $f = N_A/N$. In Leibler's mean-field theory, only two quantities turned out to be relevant parameters for the characterization of phase equilibria in a block copolymer melt: the composition f and the product χN . The phase diagram calculated from Leibler's theory is shown in Figure 3.2. A qualitative prediction can be made from this phase diagram for a fixed χN . The phase diagram shows that by increasing f one should observe, respectively, a body-centered-cubic (BCC), a hexagonal (HEX), a lamellar (LAM), an inverted HEX, and an inverted BCC microphase structure. This prediction is in agreement with the experimental results.

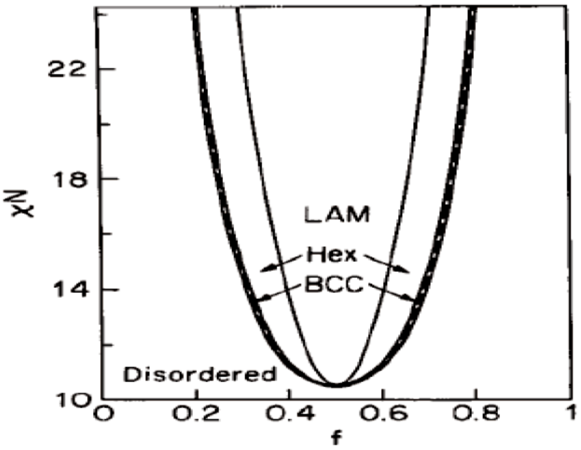

Figure 3.2 Phase diagram calculated from Leibler's mean-field theory for a diblock copolymer with all the chains having the same index of polymerization $N = N_A + N_B$ and the same composition $f = N_A/N$. The critical point occurs at $f_c = 0.5$, $(\chi N)_c = 10.495$. (Figure taken from [3])

The phase behavior of *A*-*B* diblock copolymers thus can be described in terms of the N, f and χ. All three parameters are controllable during the synthesis by choice of monomers and by stoichiometry but only χ and f are influenced by solvent uptake. When the solvent is nonselective or close to nonselective, f will be constant during vapor treatment. So here, we will only focus on χ.

3.1.2 Polymer solvent blend

In some applications or treatments, block copolymers may dissolve in solvent or blend with solvent or homo-polymers. The vapor treatment is one example that the copolymer blend with solvent. To study the mechanism of vapor treatment, it is essential to inspect the role of solvent to the copolymer *A*-*B* interactions. It is useful to consider first the ideal case in which the solvent/polymer χ parameters are equal for both blocks, $\chi_{SA} = \chi_{SB}$. An important concept for this system is the dilution approximation, which assumes that the only role of the solvent is to screen the *A*-*B* interactions, and that the solvent density is uniform throughout the system. With this approximation, the micro-phase diagram and domain size behavior for concentrated solutions are the same as for neat copolymer, except that the χ_{AB} is replaced by an effective parameter [28],

$$\chi_{eff} = \phi \chi_{AB} \tag{3.3}$$

where ϕ is the overall copolymer volume fraction. In thin film geometry, $\phi = D_{film}^{dry} / D_{film}^{swollen}$, where D_{film}^{dry} and $D_{film}^{swollen}$ are the film thickness in dry state and swollen state respectively.

The behavior of systems with slightly selective solvents is similar to that of the idealized, perfectly nonselective solvent [29, 30]. The solvent is partially partitioned between subdomains, but it is approximately uniform within each subdomain, and the variation between layers is relatively small. Nonetheless, even a slight difference can be sufficient to eliminate the small local maximum in each interphase, so that the solvent density decreases monotonically from one subdomain to the other.

3.2 The concentration dependence of T_g

3.2.1 T_g of the polymer

Polymers are glass forming materials that can undergo a glass transition and form glassy solid. When the glass transition temperature, T_g, is lower than the ambient temperature, the polymers are soft and mobile thus they can rearrange themselves to a favored state. The T_g of most polymers have been measured and can be found in literature. However, since T_g is molar mass dependence, to obtain the accurate values, the T_g's of our samples were measured by ourselves by differential scanning calorimentry [31]. The T_g of the PS and PB domains in the present copolymers are 76 °C and -89 °C, respectively.

3.2.2 T_g of the solvent

Due to the difficulty of finding a homogeneous set of experimental values for the solvents, Tg's of solvents used in this study were calculated from their melting temperatures according to a first approximation relation [32]:

$$T_g = T_m \bullet (0.6 + 0.0003 \bullet M_w) \qquad (3.4)$$

where T_m and M_w are the melting temperature and the molar mass, respectively. From the calculation, the T_g's of cyclohexane and cyclohexanone are 175 K and 162 K, respectively.

3.2.3 T_g of the polymer-solvent blend

When polymers are dissolved in or blend with solvent, the effective Tg's are influenced depending on the character of the solvent and the concentration. Usually a dilution decreases the T_g of a polymer severely. Early measurements [32] indicated that solvents with lower T_g's of their own decreased the T_g of a polymer to a greater extent. This can be seen in Figure 3.3 where the compositional variation of the T_g of polystyrene in a number of solvent is shown. Solutions of a polymer in solvents with T_g's higher than its own will usually have a greater value than that of the neat polymer [33].

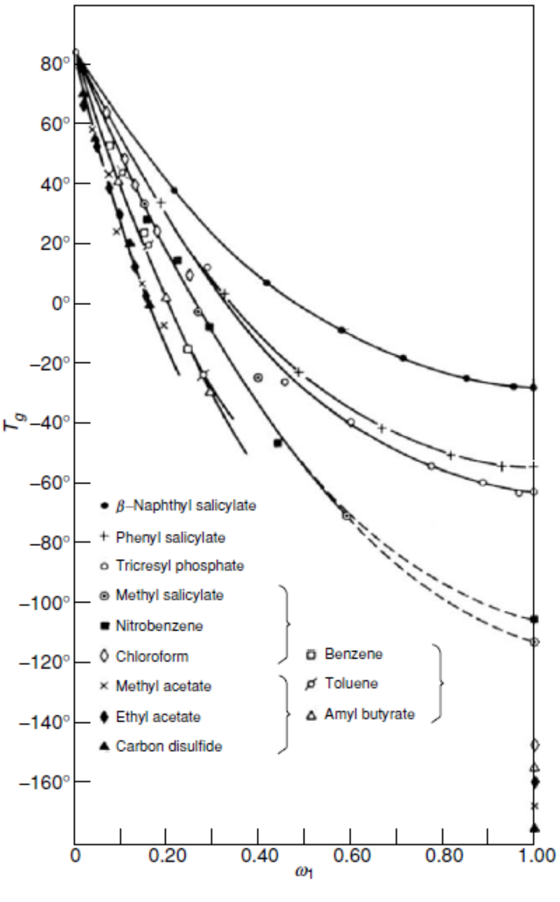

Figure 3.3 The compositional variation of the glass transition temperature T_g of polystyrene in 12 different solvents. ω_1 is the weight fraction of solvent. (Figure taken from [32])

Kelley and Bueche developed a general expression for the variation of the glass transition temperature with polymer-diluent concentration [34]

$$T_g = \frac{\phi_p \alpha_p T_{g,p} + \phi_s \alpha_s T_{g,s}}{\phi_p \alpha_p + \phi_s \alpha_s} \tag{3.5}$$

where ϕ is the volume fraction; α is the cubical thermal expansion coefficient of the fraction free volume; the subscripts *s* and *p* stand for *solvent* and *polymer*, respectively. Figure 3.4 illustrates the concentration dependence of T_g for the polystyrene-diethyl benzene system and polymethyl methacrylate-diethyl phthalate system, at $\phi_P > 0.5$, where the curves represent the prediction by Kelley-Bueche equation. The theory curves fit the experimental data very well.

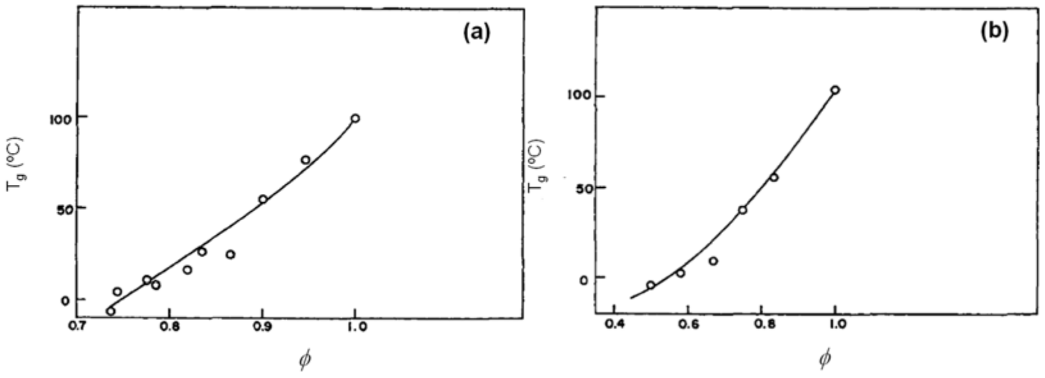

Figure 3.4 Glass transition temperatures as a function of the volume fraction of the polymers in polystyrene-diethyl benzene system (a) and polymethyl methacrylate-diethyl phthalate system (b). (Figure taken from [34])

Braun and Kovacs pointed out that when ϕ is small and the T_g is below the T_c (the cusp in a T_g - ϕ curve), such as in dilute solution, the equation [35]

$$T_g = T_{g,s} + \frac{f_{g,p}}{\alpha_s}\left(\frac{\phi_p}{\phi_s}\right) \tag{3.6}$$

predicts the variation of the glass transition temperature with volume fraction better than Equation 3.5, where $f_{g,p}$ is the fractional free volume of the polymer at its T_g.

In this work, during vapor treatment, ϕ is alway larger than 0.5. We use the term effective T_g to represent the T_g's of the polymer-solvent blend and all the them used in this study are calculated using Equation 3.5.

3.3 Selectivity of the solvent

In the first section of this chapter, we have discussed the polymer-polymer interaction parameter χ. In this section, the polymer-solvent interaction parameter χ_{p-s} will be discussed.

The miscibility of the solvent for different polymers is governed by χ_{p-s}. χ_{p-s} is modeled as the sum of entropic and enthalpic components: [36]

$$\chi_{p-s} = \chi_H + \chi_S \tag{3.7}$$

where χ_H is the enthalpic component and χ_S is the entropic component. χ_S is usually taken to be a constant between 0.3 and 0.4 for nonpolar systems: $\chi_S = 0.34$ is often used, leading to [37]

$$\chi_{p-s} = \frac{V_s}{RT}\left(\delta_s - \delta_p\right)^2 + 0.34 \tag{3.8}$$

where V_s is the molar volume of the solvent, R is the gas constant, T is the temperature, δ_s and δ_p are the solubility parameters of the solvent and polymer, respectively. According to Flory-Huggins theory, the polymer and solvent are completely miscible over the entire composition range when $\chi_{p-s} < 0.5$. [37]

It was well known that χ_{p-s} is a function of T and for most systems follows:

$$\chi(T) = a + \frac{b}{T} \tag{3.9}$$

where a contains the enthalpic interactions and b contains the entropic effects of non-random segment packing. The T dependence of χ is crucial during thermal annealing but not so important during vapor treatment in constant temperature.

One of the most important things during vapor treatment is the concentration dependence of χ_{p-s}. Though at first χ_{p-s} was considered to be independent of the concentration of the polymer, subsequent experiments have shown the necessity of treating χ_{p-s} as a function of composition [38, 39].

Based on the lattice theory [40], the following expression for the Flory-Huggins parameter was deduced [41]:

$$\chi_{p-s} = \alpha + \frac{\beta(1-\gamma)}{(1-\gamma\varphi_2)^2} \tag{3.10}$$

where α and γ are constants within a certain temperature range and β varies with *T*.

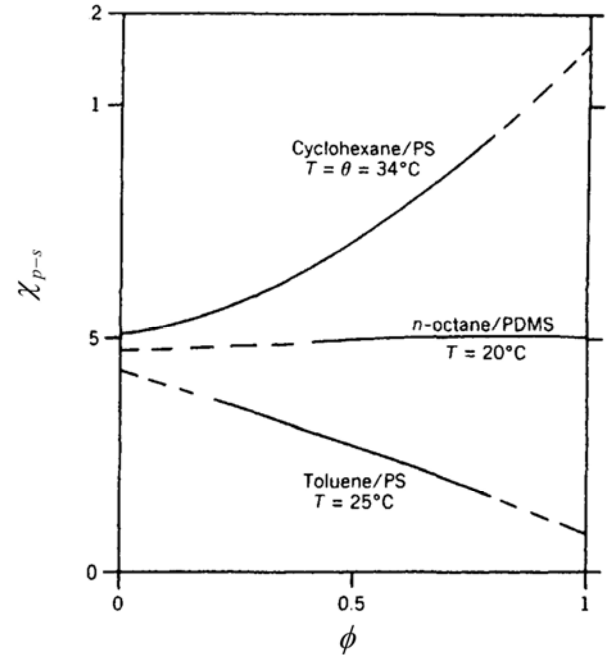

Figure 3.5 Examples for the variation of χ_{p-s} with the volume fraction of polymer, ϕ, for the systems of cyclohexane/polystyrene (PS), n-octane/poly(dimethyl siloxane) (PDMS) and toluene/PS at the indicated temperatures. Figure taken from [41].

According to experimental information, three characteristic behaviors can be distinguished (see Figure 3.5) [41]:

1. Very often, χ_{p-s} increases greatly with polymer concentration, particularly in the case of poor solvents.
2. In some cases, χ_{p-s} seems to be independent of composition, as proposed by the original Flory-Huggins theory. These findings mainly concern good solvents.
3. In a few case, mostly with highly exothermal systems, χ_{p-s} decreases with concentration.

In this study, CHX and CHXO are used as solvent for vapor treatment. χ_{PS-CHX} follows the first behavior described above and is shown in Figure 3.5. χ_{PB-CHX} increases slightly from 0.26 to 0.36 for ϕ decreasing from 0.8 to 0 (the 3rd behavior described above). $\chi_{PS-CHXO} = 0.4$ and $\chi_{PB-CHXO} = 0.7$ are obtained using Equation 3.8, but the ϕ dependence is not found from literature.

Chapter 4

Experimental

4.1 The samples

Two kinds of poly(styrene-*b*-butadiene) (P(S-*b*-B)) diblock copolymers, namely SB12 and SB4908, are used in this study. SB12 was synthesized by anionic polymerization [42]. Its molar mass is 22.1 kg/mol, which corresponds to a degree of polymerization N = 374 and it has a polydispersity index, PDI of 1.05 [31]. The PB volume fraction is 0.49 ± 0.01. In bulk, the polymer forms lamellae with a lamellar thickness of 189 ± 1 Å. The Flory-Huggins segment-segment interaction parameter is $\chi = A/T + B$ with A = 21.6 ± 2.1 K and B = -0.019 ± 0.005 [31]. At room temperature, $\chi N = 20$, the sample is thus in the intermediate segregation regime [43]. The order-to-disorder transition temperature (T_{ODT}) is 181 ± 2 °C. The glass transition temperatures of PS and PB in the present copolymer are T_g = 76°C and -89°C respectively, as measured by differential scanning calorimetry [31].

SB4908 is a commercial product from *Polymer Source Inc., Canada*. Its molar mass is 28.0 kg/mol (15.0 kg and 13.0 kg for PS and PB respectively), which corresponds to a degree of polymerization N = 474. It has the same PDI of 1.05 as SB12. The PB volume fraction is not provided by the supplier and f_{PB} = 0.51 is calculated from the molar masses of each block. Since SB4908 is very similar to SB12 and χ depends only on the pair of monomers chosen, we assume that the Flory-Huggins segment-segment interaction parameter, χ, is the same for both. Thus, at room temperature, $\chi N = 25$, the sample is in the intermediate segregation regime [43].

To prepare thin films, the block copolymers were first dissolved in toluene then the polymer solution was poured onto the Si substrates until these were completely wet. Films were spin-coated at 3000 rpm for 30 s and stored in vacuum at room temperature or at 60 °C for one day to remove the residual solvent. The Si substrates were cut from Si(100) wafers with a dimension of 2 × 4 cm^2 and cleaned by UV or acid bath. For the latter, the Si substrates were cleaned as follows: sonication in dichloromethane at 35 °C for 15 min, water rinsing for 5 min, and then soaking in the cleaning bath at 80 °C for 15 min. The cleaning solution was composed of 100 mL of 96% H_2SO_4, 35 mL of 35% H_2O_2, and 65 mL deionized water. The cleaned substrates were further rinsed in deionized water for 10 min and finally spin-dried. At last the substrates were rinsed and spin-dried with methonal and aceton chronologically to decrease the surface energy.

4.2 White light interferometer

4.2.1 Methods

The white light interferometer “Filmetrics F20” (Filmetrics Inc., San Diego) is used to measure the film thickness. The Filmetrics F20 can measure the thickness and optical constants (*n* and *k*) of transparent and semi-transparent thin films. Measured films must be optically smooth and between 10 nm and 50 µm thick. Since our block copolymer thin films have a film thickness between 90 nm and 500 nm, it is ideal in our case.

The basic idea behind the technique is to reflect a batch of light with different wavelength from a flat surface or interface and to then measure the intensity of the light reflected in the specular direction (reflected angle equal to incident angle). Based on Fresnel equations, when light makes multiple reflections between two or more parallel surfaces, the multiple beams of light generally interfere with each another, resulting in net transmission and reflection amplitudes that depend on the light-wavelength [44]. Therefore the reflection spectrum shows a series of fringes of which the positions and the amplitude are mainly dependent on the film thickness, surface roughness and optical constants (*n* and *k*). By fitting with a model system containing layers of varying refractive index/thickness, the thickness/refractive index values can be acquired.

4.2.2 Setup

The Filmetrics F20 is composed of a spectrophotometer (with light source), a set of fiber-optic cables and a lens assembly (Figure 4.1). The lens assembly can be fixed on the cover of the sample cell where a glass window allows the light to transmit. The fiber-optic cable contains 7 fibers: a single detection fiber surrounded by 6 illumination fibers. The measurement spot size is the intersection of the illuminated area with the projected image of the detection fiber.

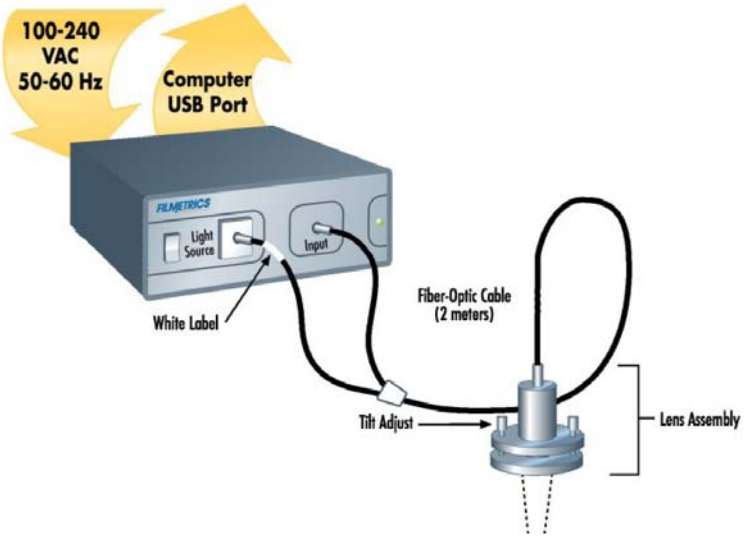

Figure 4.1 Setup configuration for the Filmetrics F20 (Figure taken from the operation manual)

4.2.3 Data analysis

The F20 is able to determine thin film characteristics by first carefully measuring the amount of light reflected from the thin film over a range of wavelengths, and then analyzing this data by comparing it to a series of calculated reflectance spectra using the software "FILMeasure" (as shown in Figure 4.2). The P(S-*b*-B) thin film is set to be homogeneous with the reflective index, *n* = 1.5. During the measurement, the film thickness, *d*, and roughness, *r*, are fitted by the software.

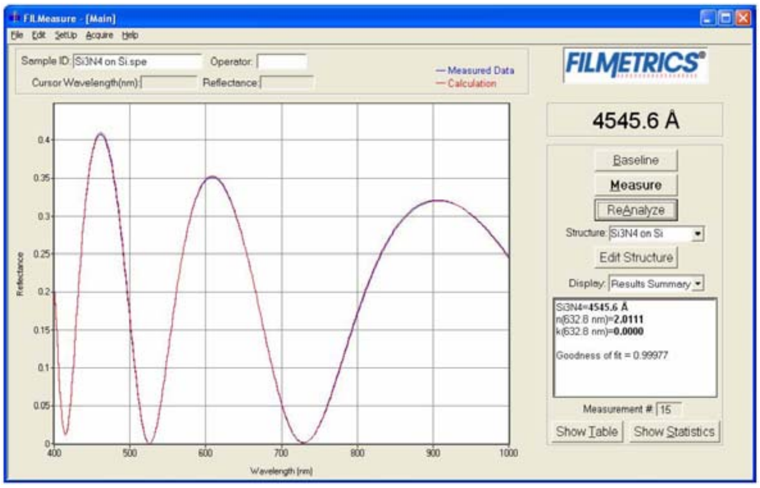

Sample ID: Si3N4 on Si.spe
Operator:

4545.6 Å

Structure: Si3N4 on Si
Display: Results Summary

Si3N4=**4545.6 Å**
n(632.8 nm)=**2.0111**
k(632.8 nm)=**0.0000**

Goodness of fit = 0.99977

Measurement #: 15

Figure 4.2 An example of the FILMeasure software main window. The blue curve is from the experimental data and the red curve is the fitting. (Figure taken from the operation manual)

4.3 X-ray reflectivity

4.3.1 Methods

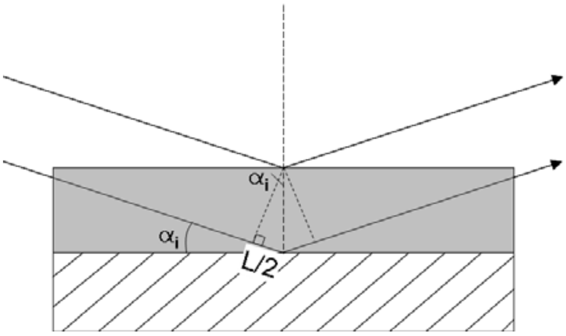

Figure 4.3 Illustration of specular reflectivity.

X-ray reflectivity (XR) is a surface-sensitive analytical technique used in chemistry, physics, and materials science to characterize surfaces, thin films and multilayer [45, 46]. The basic idea behind the technique is to reflect a beam of x-rays from a flat surface and then measure the intensity of x-rays reflected in the specular direction. For example, when X-rays impinge on a flat material (Figure 4.3), the surface reflected beam and the thin film/substrate reflected beam may interference. When the difference of the X-ray path lengths, L, fulfills Bragg's law:

$$L = 2D_{film} \sin \alpha_i = n\lambda \tag{4.1}$$

where D_{film} is the film thickness, α_i is the incidence angle, λ is the wavelength and n = 1,2,3…, the two reflected beams will be constructive and the *Kiessig fringes* are seen. Therefore the film thickness can be deduced from the period of the *Kiessig fringes*. The roughness of the thin film is deduced from the amplitudes of the fringes. When there are repeated sublayers within the thin film, additional *Bragg peaks* are superposed on the *Kiessig fringes*. The thickness of the sub layers can be deduced from Equation 4.1 with the D_{film} replaced by the sub layer thickness.

4.3.2 Setup

XR experiments were carried out at CHESS beamline D1 using the collimating slits, goniometer and sample environment of the GISAXS experiments. The detector was an ion chamber with an aperture of 50 mm height and 13 mm width mounted a few cm in front of the CCD camera. The direct beam spilling over the sample surface at low angles was blocked by a blade in front of the ion chamber. The advantage of using this GISAXS experiments sample environment is obvious: the GISAXS measurement and the XR measurement can be combined and be switched easily during the vapor treatment without touching the sample.

The XR measurements were only carried out for the experiment described in Chapter 5. The measuring time was 1 second per point, and measuring the whole curve took ~10 min. The electronic background of the detector was measured and subtracted from the data.

4.3.3 Data analysis

For fitting models of the scattering length density profiles, the software Parratt32 (HMI Berlin) was used. Parratt32 is a program to calculate the optical reflectivity of neutrons or x-rays from flat surfaces. The calculation is based on Parratt's recursion scheme for stratified media [47].

In the fit, the Si substrate is set to be homogeneous with indefinite thickness. A SiO_x thin layer is on the top of the substrate. For lamellar thin film with short-range order, the main part of the polymer film is set to be homogeneous, while for thin film with long-range order of parallel lamellae, the main part of the polymer film is set to be repeating PS and PB layers. In both cases, a top layer with a lower SLD stands at the surface. Such a layer may be attributed to the inhomogeneity of the film thickness after preparation or to terrace formation in the upper lamellar layer [48].

4.4 GISAXS

4.4.1 Methods

Grazing-incidence small-angle X-ray scattering (GISAXS) is a versatile tool for characterizing nanoscale density correlations and/or the shape of nanoscopic objects at surfaces, at buried interfaces, or in thin films [49-51]. As a hybrid technique, GISAXS combines concepts from transmission small-angle X-ray scattering (SAXS) [52] and from grazing incidence diffraction (GID) [46]. Applications range from the characterization of quantum dot arrays [53] and growth instabilities formed during in-situ growth [54], as well as self-organized nanostructures in thin films of block copolymers [55], silica mesophases [56], and nanoparticles [57]. In general, GISAXS can be applied to characterize self-assembly and self-organization on the nanoscale in thin films.

Similar to SAXS, GISAXS is using a reflection geometry but suited for thin films. In GISAXS, the beam does not transmit through the sample but impinges under a grazing angle (< 1°) and the reflected and scattered intensities are recorded with a 2D detector. Thus, big advantages of GISAXS over SAXS are the high sensitivity to the surface structures and the improvement of the resolution limit. Varying the distance between the sample and the detector, structures of 5 nm to 15 μm can be resolved by GISAXS. The scattering data are analyzed in a similar way as done with SAXS. The basic experimental set-up is shown schematically in Figure 4.4. GISAXS also shares elements of the scattering technique of diffuse reflectivity such as the Yoneda peak at the critical angle of the sample, and the scattering theory, the so-called distorted wave Born approximation (DWBA) [58-60].

In summary, there are two advantages of GISAXS over SAXS: one advantage is that GISAXS gets rid of the background scattering from the substrate i.e. the X-ray does not need to traverse the substrate. This is crucial in thin film geometry. The other big advantage is the improvement of the resolution limit. In SAXS, the direct beam needs to be shielded on the detector to avoid damage by the high intensity, which limits the access to very small values of the scattering vector q, i.e, large structural length scales. GISAXS overcomes this problem by reflection, because the direct beam is far from the interesting region on the detector and as a result, a better resolution can be achieved as compared to a transmission experiment.

4.4.2 Setup

The GISAXS measurements were performed at two different beamlines. One is at beamline D1 at the Cornell High Energy Synchrotron Source (CHESS) at Cornell University in Ithaca, NY, USA. The other was at beamline BW4 at the DORIS III at HASY LAB in the Deutsches Elektronen-Synchrotron (DESY) in Hamburg, Germany. At both beamlines, the sample cell was mounted horizontally on a goniometer and the X-rays hit the sample surface with an incidence angle between 0.14° and 0.18°. A CCD camera behind the sample recorded the scattering photons. The sample to detector distances were selected between 1.76 m and 1.97 m. Exposure times were controlled by a fast shutter in the incident beam. The setup is shown schematically in Figure 4.4.

Beamline D1 is located on a hard-bent dipole magnet of the CESR storage ring and uses a W:C multilayer monochromator with about 1.5 percent band path providing 10^{12} photons per mm^2 and sec at a photon energy of 8 keV. Two collimation slits and a guard slit condition the beam before it impinges onto the sample surface. A CCD camera with pixel sizes of 46.9 × 46.9 μm^2 is used. The image size is 1024 × 1024 pixels [55].

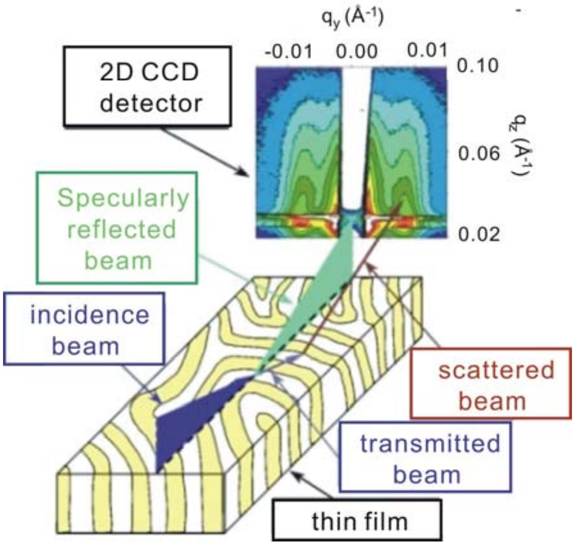

Figure 4.4 The basic experimental setup of GISAXS. The sample is placed horizontally. The 2d detector represents the q_y-dependence along the horizontal axis and the q_z-dependence along the vertical axis. The scattered intensity distribution on the detector is presented in logarithmic scale. The scattering pattern shows the diffuse scattering with a vertical shadow in the middle due to the rod-like beamstop in front of the detector. (Figure taken from [61])

The Beamline BW4 at the DORIS III storage ring at HASYLAB has been designed as an ultra-small-angle x-ray scattering (USAXS) instrument with minimum scattering angles on the order of 0.01°. BW4 achieves a maximum USAXS resolution of $d_{max} < 1$ μm. The x-rays are produced by a wiggler (N=19 periods, K=13.2). The x-ray beam is monochromatized using a fixed exit double Si(111) monochromator and focused horizontally and vertically using a fixed cylindrical mirror and a plane mirror with a mirror bender, respectively [62]. The selected wavelength was $\lambda = 1.381$ Å. The beam divergence in and out of the plane of reflection was set by two entrance cross-slits. To operate a microbeam the X-ray beam was moderately focused to the size of (H × B) 25 × 47.5 μm^2 by using an assembly of refractive beryllium lenses. The sample was placed horizontally on a goniometer. The direct beam was blocked by a diode beam stop in front of the detector to protect the detector from high intensity beam. A second, point-like moveable beam stop was also used to block the specular peak on the detector. The light path of the incoming and scattered beam was evacuated to avoid scattering from air.

4.4.3 Data analysis

4.4.3.1 Lamellar orientation

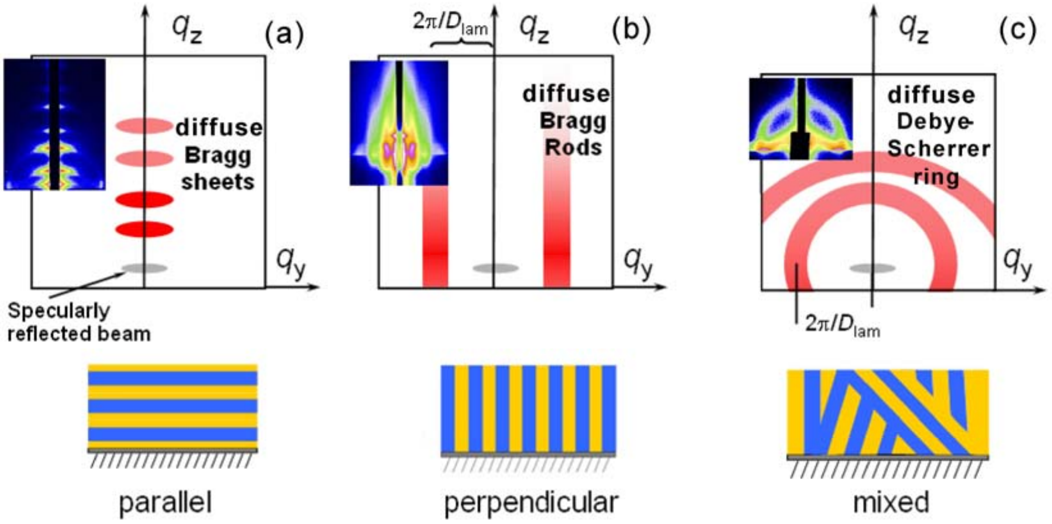

Figure 4.5 Schematic GISAXS images with the real images in the top-left corner for lamellar block copolymer thin films with the lamellar orientation parallel to the film surface (a), perpendicular to the film surface (b) and having mixed/random orientation (c). The names of the scattering peaks are indicated in each image.

Figure 4.5 shows the schematic GISAXS images and the real GISAXS images in the top-left corner of each schematic image for lamellar block copolymer thin films. The inner structure of thin film is indicated below each image. Different scattering patterns namely diffuse Bragg sheets (DBS's), diffuse Bragg rods (DBRs) or diffuse Debye-Scherrer rings (DDSR's) are observed for different lamellae orientations as shown in the figure.

4.4.3.2 Two branches of scattering

From Figure 4.6 it is seen that the DBS's appear in pairs in each order. One branch of the DBS's comes from the direct beam (namely 'M' branch) and the other branch of the DBS's come from the reflected beam from the substrate (namely 'P' branch) [63]. For DBR's, these two branches overlap at:

$$q_y = \frac{2\pi}{D_{lam}^{perp}} \tag{4.2}$$

where D_{lam}^{perp} is the lamellar thickness of the lamellae perpendicular to the film surface. For the DBS's the two branches separate at:

$$q_z = k_{iz} + \sqrt{k_{cP}^2 + \left[\frac{2\pi m}{D_{lam}^{par}} \pm \sqrt{k_{iz}^2 - k_{cP}^2}\right]^2} \tag{4.3}$$

where $k_{iz}=k_0\sin\alpha_i$ and $k_{cp}= k_0\sin\alpha_{cp}$ with $k_0=2\pi/\lambda$. α_i is the incidence angle of the X-ray beam with respect to the film surface. α_{cp} is the critical angle of total external reflection of P(S-*b*-B), which is a function of the wave length. D_{lam}^{par} is the lamellar thickness of the parallel lamellae. The 'p' branch and 'm' branch correspond to the 'Plus' and 'Minus' sign in Equation 4.3, respectively [63].

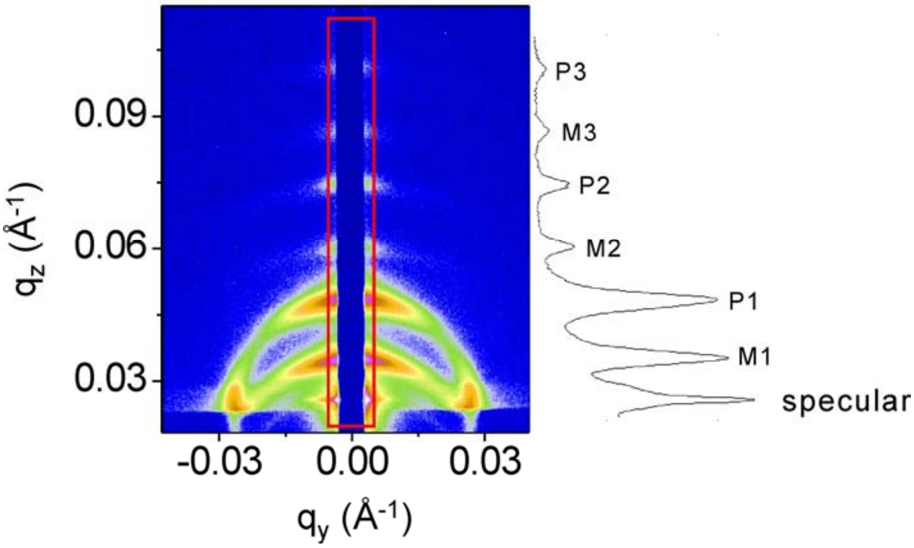

Figure 4.6 Typical GISAXS image for lamellar block copolymer thin film with lamellar orientation dominantly parallel to the film surface (left) and its intensity profile along q_z axis (right). The red box in the GISAXS image indicates the region of integration used for obtaining the intensity profile.

4.4.3.3 Fitting of the DBS's

A program named *Layers* [64] was written according DWBA model [65] to fit the peak position of the DBS's. The *Layers* is designed for thin films with parallel *A*-*B* repeating layers. The thickness of *A* and *B*-layer together with α_i can be fitted. Since in the program, the parallel layers are assumed to be infinitely long and perfect, there is no intensity decay with increasing q_z. Therefore, it can only fit the peak position but not the peak heights/intensities.

4.4.3.4 Scattering depth

The penetration or information depth of the X-rays is controlled by α_i and α_f /q_z. When α_i is smaller than α_c (critical angle of the polymer), the penetration depth is less than 5 nm, which is independent of α_f [66]. To investigate the inner structure of a thin film thick than 5 nm, the α_i must be larger than α_c . However, in this case, the situation is qualitatively different. The upper limit of the scattering length is then merely determined by photoelectric absorption and therefore increases continuously with α_f [66].

In our study, the thin films are always thicker than 90 nm and $\alpha_i 's$ are always larger than α_c . Therefore, the scattering depth is a function of α_f (or q_z), i.e. the low-q_z scattering comes mainly from the film surface while the high-q_z scattering comes mainly from the film bottom.

Chapter 5

Vapor treatment with saturated CHX

5.1 Idea

Vapor treatment has been shown to be an effective way to anneal defects and increase the long-range order of the nanostructure of block copolymers. Despite extensive studies of resulting structures, the underlying molecular processes occurring during vapor treatment are still not well understood. It would be desirable to know which conditions –vapor pressure, duration of treatment time etc. – are optimum for obtaining the desired structure. Moreover, apart from showing fundamentally interesting phenomena, a detailed understanding of the processes during restructuring is needed for the optimization of annealing procedures and for design of sensors for volatile solvents, for instance. In this work, we carried out GISAXS measurements during vapor treatment with saturated CHX vapor. Using real-time, in-situ GISAXS, the swelling and the rearrangement of the lamellae were followed with a time resolution of a few seconds, and the underlying processes on the molecular level were revealed.

5.2 Experimental

The polymer used in this study is the block copolymer SB12 (see § 4.1). In-situ vapor treatment with CHX was performed using the sample cell shown in Figure 5.1. Its volume amounts to ~110 ml. Up to 3 ml of solvent can be injected remotely through a long Teflon capillary into the solvent reservoir at the bottom of the cell, i.e. ~2 cm below the sample. A time series was initiated such that 2-3 initial GISAXS images were taken before injection, and the time series continued during injection and subsequent solvent annealing. After 30 min, when the experiment was finished, there was still solvent present in the cell, i.e. the vapor pressure was close to saturation during the experiment.

A light bulb at the top of the cell heats the cell slightly and thus prevents condensation of solvent vapor on the sample and on the Kapton windows. In order to avoid beam damage of the polymer film, the sample was moved sideways after each exposure, such that a pristine spot was illuminated in each measurement. A second scan of the same region was started after 19 min. The results do not show any signs of beam damage from the first run. GISAXS images were recorded every 15 s (10 s for measurement and 5 s for CCD read-out, data storage and change of sample position) for the first 19 min and every 25 s (extra 10 s waiting time) afterwards.

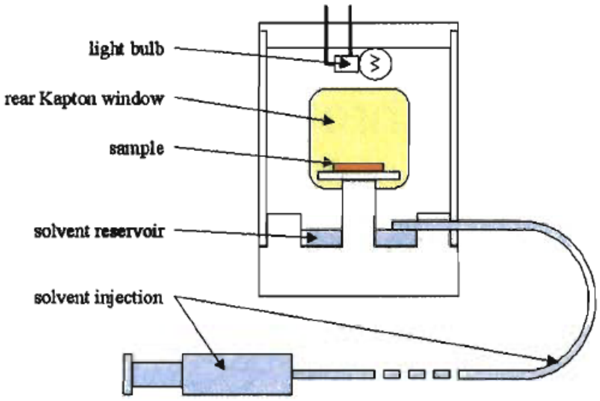

Figure 5.1 Cross section through the sample cell used for vapor treatment of P(S-*b*-B) thin film, viewed in beam direction. The X-ray beam enters and exits the cell through thin Kapton windows. CHX solvent can be injected remotely into a reservoir below the sample. A small light bulb mounted on the top of the cell provides a small amount of heating to prevent condensation of solvent vapor on the sample and on the windows. (Figure taken from [61])

5.3 Results

We first discuss the film structure in the dry state and then describe the structural changes when the sample is subject to CHX vapor.

5.3.1 Structure of the as-prepared film

5.3.1.1 X-ray reflectivity

The film thickness of the as-prepared sample was determined using XR. Figure 5.2a (lower curve) shows the measured XR curve together with a fit of a layer model which is shown in Figure 5.2b (black curve). The curve shows a number of Kiessig fringes. In the fit, the scattering length density (SLD) of Si was fixed at 2.07×10^{-5} Å^{-2}. The SLD and thickness of the SiO_x layer were left as fitting parameters: An SLD value of 2.33×10^{-5} Å^{-2} and thickness of 27

Å were obtained, respectively. From modeling, the main part of the polymer film appears homogeneous with an SLD of 8.99×10^{-6} Å^{-2} which is exactly the expected value of P(S-*b*-B). No inner layered structure is observed, which is consistent with the GISAXS results below. Only at the surface, a top layer (~180 Å) with a lower SLD is found. Such a layer may be attributed to the inhomogeneity of the film thickness after preparation or to island formation in the upper lamellar layer [48]. As shown below, the lamellar thickness in the thin film is $D_{lam}^{par} = 178 \pm 5$ Å, thus similar to the thickness of the top layer. The thickness of the homogeneous part of the film is 1016 ± 10 Å, which corresponds to 5.4 × D_{lam}.

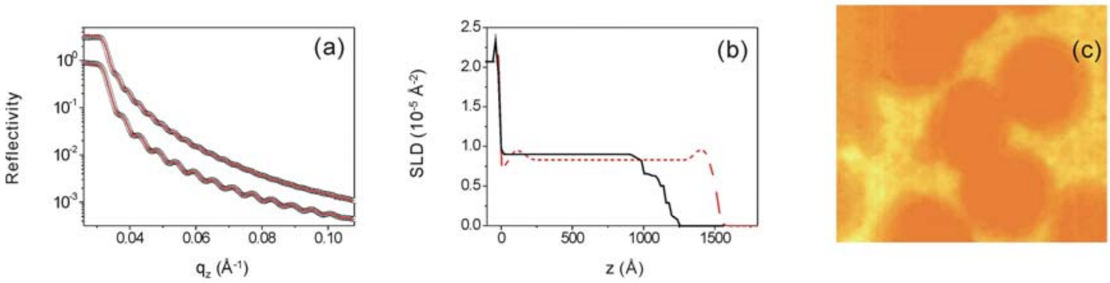

Figure 5.2 (a) XR curves of the as-prepared sample (lower curve) and the fully swollen film (upper curve). Symbols: experimental curves; lines: fitted model curves. (b) Models used to fit the XR curves. Black full line: as-prepared film; red dashed line: fully swollen film. The substrate surface is located at z = 0. (c) AFM height image of the asprepared sample. Image size 5×5 μm^2. The color scale runs from 45 nm (orange) to 75 nm (light yellow).

5.3.1.2 GISAXS

Figure 5.3 shows a 2D GISAXS image of the as-prepared film (measurement time 10 s). It features two DDSR's and a weak and broad DBS. A short-range ordered, microphase-separated morphology was thus present in the film, i.e. lamellae having a broad distribution of orientations. The two DDSR's are due scattering of the beam specularly reflected (upper ring, 'P') from the substrate and scattering of the direct beam (lower ring, 'M'). Due to dynamical effects, the rings are enhanced in the region between the Yoneda peak of the polymer and of the substrate. A certain fraction of the lamellae features a parallel orientation, as evident from the appearance of the DBS. The intensity of this DBS does not follow the general decline of the ring intensity towards high q_z.

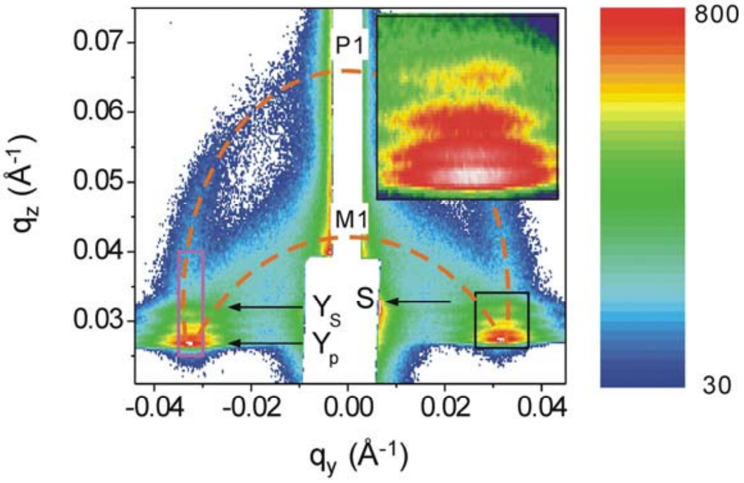

Figure 5.3 2D GISAXS image of the as-prepared sample at $\alpha_i = 0.18°$. The measuring time was 10 s. The regions of low intensity (white rectangles in the center) are due to the rod like beam-stop and the lead tape. Arrows mark the positions expected for the Yoneda peaks of the polymer (Y_P) and the Si substrate (Y_S). The two ellipses indicate the two diffuse Debye-Scherrer rings, centered on the direct beam and the specularly reflected beam(marked "S").M1 and P1 stand for the minus and the plus branch of the first-order DBS and DDSR (eq 1). The inset shows a zoom of the black rectangle. The left magenta box indicates the range of integration for the intensity profile in Figure 5.4.

We have previously observed that the P(S-*b*-B) diblock copolymer under study has a parallel lamellar structure in thermal equilibrium on Si wafers cleaned by detergent solution, water and toluene [65, 67]. In contrast, the present sample was spin-cast onto a UV treated Si wafer. We conclude that the substrate properties and possibly details regarding the actual spin-coater used have an influence on the degree of lamellar orientation.

From the present single 2D GISAXS image, the lamellar thickness cannot be determined with high precision because the DBS is broadened along q_z and because the specularly reflected beam is shielded by lead tape. It becomes possible, though, using a series of GISAXS images taken at several values of α_i between 0.05° and 0.5° (Figure 5.4a-d). To precisely determine the position of the specularly reflected beam (which is a direct way for the exact determination of α_i), the lead tape was removed, thus only shorter measuring times were possible, resulting in less good statistics. For $\alpha_i = 0.11°$, only very weak scattering is observed in the Yoneda band (Figure 4a). This incidence angle is below $\alpha_{cp,}$ thus only scattering from a thin layer beneath the film surface can be observed [68]. The absence of scattering indicates that close to the film surface, no pronounced, surface-induced structure is present. The images with α_i between α_{cP} and α_{cS} and slightly above (Figure 5.4b, c) show the same features as the image shown in Figure

5.3. For α_i significantly larger than α_{cS} (Figure 5.4d), the diffuse scattering is very weak, because the reflectivity of the film/substrate interface is low.

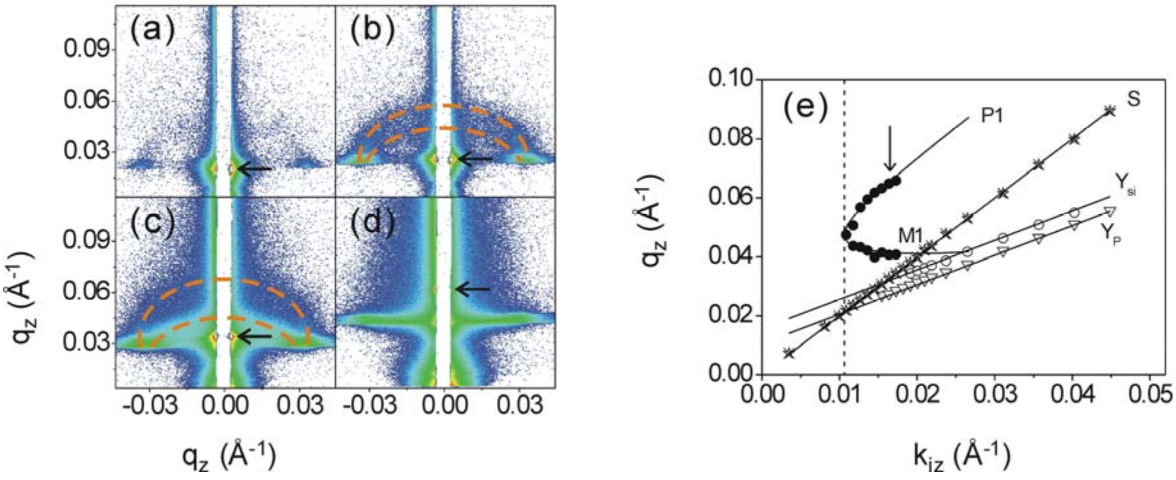

Figure 5.4 2D GISAXS images of the as-prepared sample at α_i = 0.11° (a), 0.14° (b), 0.19° (c) and 0.34° (d). Measuring times were 0.3 s for (a-c) and 10 s for (d). The arrows indicate the position of specularly reflected beam. The logarithmic intensity scale runs from 3 to 2000 cts for all images. (e) Resulting q_z positions of the specularly reflected beam (stars, marked S), the Yoneda peaks of the polymer (open triangles, Y_p) and of the Si substrate (open circles, Y_S) as well as the q_z values of the DDSR's (filled circles) as a function of k_{iz} together with fits of Equation 4.3 to the minus and the plus branch of the first order (marked M1 and P1, solid lines). The vertical dashed line marks the resulting k_{cP}. The arrow indicates the incidence angle used during vapor treatment.

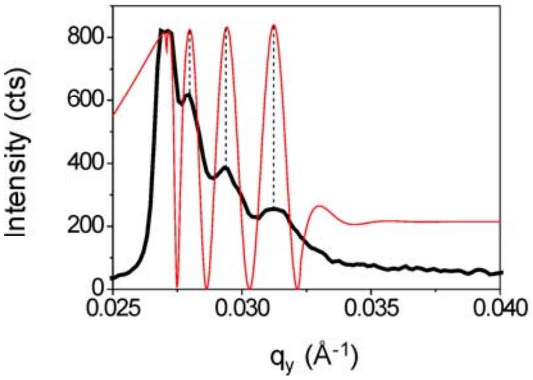

Figure 5.5 Black thick line: Intensity profile along q_z through the DDSR of the as-prepared sample at α_i = 0.18°. Red thin line: Fit of the profile of a homogeneous, flat film, see text.

Ellipses were constructed to the rings of diffuse scattering, and the lengths of their half axes along q_z are given as a function of k_{iz} (i.e. α_i) together with the fitting curves (Equation 4.3) in Figure 5.4e. The q_z values of the specularly reflected beam and of the Yoneda peaks from the polymer and the Si substrate are given as well. From the fits, we obtain $D_{lam}^{par} = 178 \pm 5$ Å, and k_{cP} = 0.0105 Å^{-1} (vertical dashed line) which corresponds to the mean value of k_{cP} for a 50/50 vol/vol mixture of pure PS and pure PB. From the length of the q_y half axes of the ellipses, the average D_{lam}^{perp} was found to be 188 ± 3 Å, i.e. the value is practically independent of α_i. D_{lam}^{perp} is thus equal to the bulk value (189 ± 1 Å). In contrast, D_{lam}^{par} is 6 % lower than in the bulk. This effect has been previously observed by us [67]. The film thickness of the as-prepared sample and the thickness during swelling could be determined from the period of oscillations and the positions of the maxima in the intensity profiles along q_z through the DDSR's (Figures 5.3 and 5.5) as described in the Experimental Section. The positions of the maxima could be recovered very well. However, whereas in the model, the amplitude of the oscillations between the Yoneda peaks of the polymer film and the substrate are constant, the experimental curve decays with increasing q_z and shows less pronounced oscillations. We attribute this difference to the high roughness of the film surface (see XR result above) and to the presence of internal structure in the sample which is not included in the model. Fitting the position of the maxima, we obtain a film thickness of 970 ± 30 Å in the dry state (Figure 5.5). which agrees well with the value found by XR (1016 ± 10 Å). This fast method of film thickness determination from the GISAXS images was applied during vapor treatment, where XR measurements would take too long.

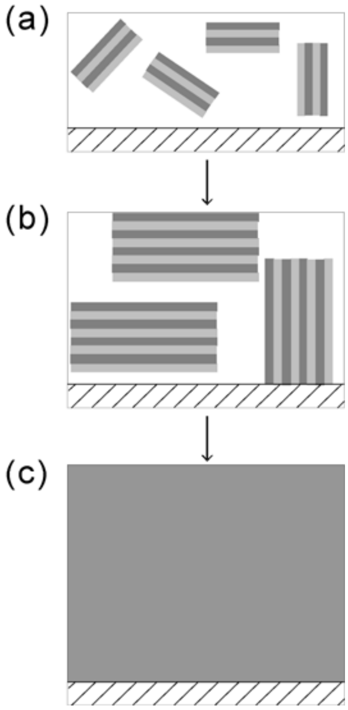

Figure 5.6 Sketch of the structure of the as-prepared sample (a), the transient state (b) and the final, disordered state (c). The different shades of grey indicate the PS and PB parts of the lamellae. For clarity, only a few lamellar domains are shown. The substrate is marked by dashes.

We conclude that, in the dry state, the film consists of domains of lamellae with short-range order and a wide distribution of orientations. A certain preference for the parallel lamellar orientation is found, as expected. D_{lam}^{perp} is very similar to the bulk value, whereas D_{lam}^{par} is 6 % smaller than in the bulk. We summarize the structure of the as-prepared film in Figure 5.6a.

5.3.2 Structural changes during vapor treatment

Cyclohexane (CHX) was used as the solvent for vapor treatment. It is known to be a good solvent for PB and a θ solvent for PS. It is thus selective for PB, i.e. $\chi_{PB-CHX} < \chi_{PS-CHX}$. Therefore, the volume fraction of CHX in PB is expected to be higher than in PS. Moreover, χ_{PB-CHX} and χ_{PS-CHX} both depend on ϕ [69]. The dependence is much weaker for χ_{PB-CHX} than for χ_{PS-CHX}: χ_{PB-CHX} increases slightly from 0.26 to 0.36 for ϕ decreasing from 0.8 to 0, whereas χ_{PS-CHX} decreases from 0.92 to 0.51 in the same ϕ range. The values at $\phi = 0$ are calculated from the solubility parameters [70] and are consistent with the ϕ dependence. This means that during CHX vapor uptake, the selectivity of CHX varies. In the final state of swelling, where $\phi \approx 0.55$, the χ-values are $\chi_{PS-CHX} \approx 0.8$ and $\chi_{PB-CHX} \approx 0.3$. For the poly(Styrene-*b*-isoprene)/CHX system with $\chi_{PS-CHX} = 0.59$ and $\chi_{PB-CHX} = 0.39$, an uneven distribution with $\phi_{PS} = 0.71$ and $\phi_{PB} = 0.48$ was predicted (Figure 13a in Ref. 40). In our case, the selectivity, i.e. the difference of χ-values is higher throughout the entire experiment, thus a more uneven distribution is expected. The values of the volume fraction of CHX in the PS and PB domains cannot, however, be calculated in a straightforward manner.

Upon injection of liquid CHX into the sample cell, drastic changes of the GISAXS images are observed (Figure 5.7): (i) During the first ~7.5 min, the radii of the DDSR's vary, while intensities and the DBS's are approximately unchanged. (ii) 7.5 min to 13.5 min after injection, the DBS's get more pronounced and sharper, whereas the intensities of the DDSR's decrease drastically. (iii) After 13.5 min, the intensity along the DDSR reappears and its intensity becomes more evenly distributed. A transient state has thus been revealed. It is observed more clearly in the intensity profiles through the DDSR's and the DBS's (Figure 5.8): (i) For times shorter than 7.5 min, the profile through the DBS is flat (Figure 5.8a), and the profile through the DDSR shows a flat and broad peak at q_y = 0.0323 $Å^{-1}$ (Figure 5.8b). We conclude that, in this time regime, the microphase-separated structure stays short-ranged (Figure 5.6a). (ii) Between 7.5 min and 13.5 min, both profiles display well-pronounced peaks. This indicates the appearance of more long-ranged lamellar order (Figure 5.6b). (iii) For times longer than 13.5 min, the profile through the DDSR's display a weak and broad peak reminiscent of the

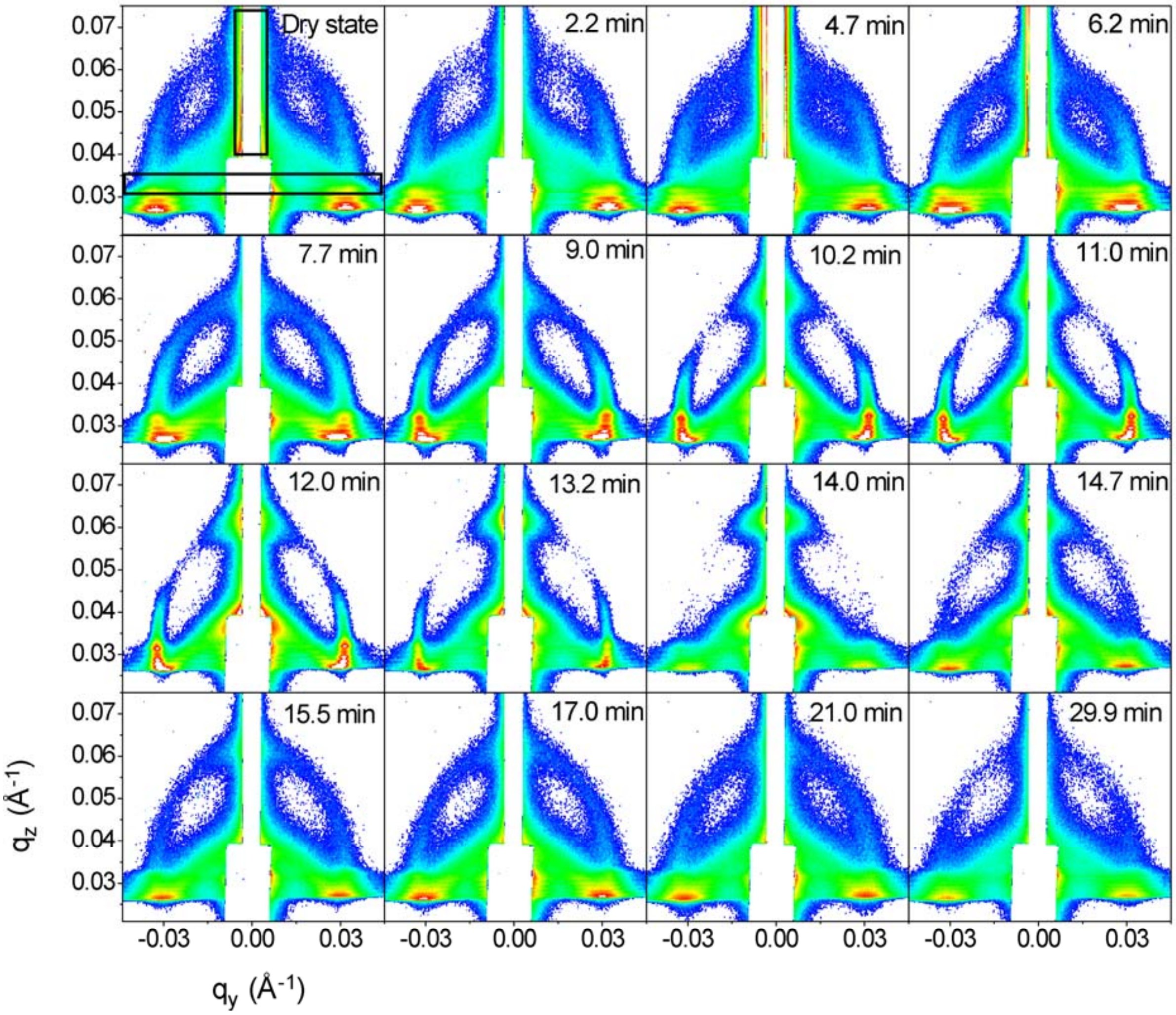

Figure 5.7 GISAXS images of the film during treatment with saturated CHX vapor for the times given in the figures. $\alpha_i = 0.18°$. The logarithmic intensity scale runs from 30 to 600 cts for all images. The boxes in the image of the dry state indicate the regions of integration used for obtaining the profiles along q_z (Figure 5.8a) and along q_y (Figure 5.8b).

correlation peaks observed in the disordered state [26, 31, 43] and the DBS's disappear (Figure 5.6c). We will discuss the transition to the disordered state below.

In the following, we will quantify the thicknesses of the differently oriented lamellae, D_{lam}^{par} and D_{lam}^{perp} and compare these to the changes in the film thickness.

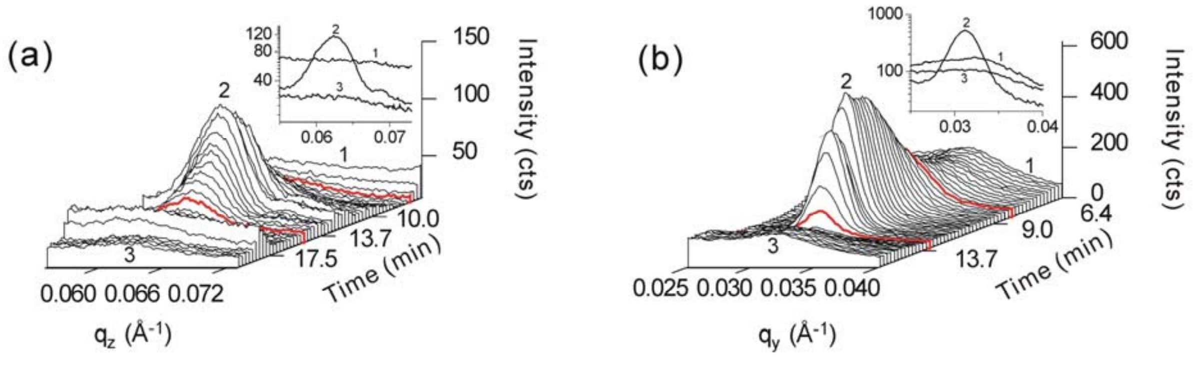

Figure 5.8 Intensity profiles along q_z, i.e. through the DBS (P1) (a) and along q_y i.e. through the DDSR (P1) (b) from the images in Figure 6 as a function of treatment time. Representative profiles from the three time regimes marked 1-3 are shown in the inserts. The thick red lines mark the times 7.5 min and 15 min in (a) and 7.5 min and 13.5 min in (b), i.e. when the peaks appear and vanish.

5.3.2.1 Lamellar thickness

The lamellar thickness of the parallel lamellae, D_{lam}^{par}, is deduced from the q_z position of the DBS's. These can directly be read off from the peaks in the intensity profiles (Figure 5.8a) for vapor treatment times between 7.5 min and 13.5 min. For earlier and later times, however, the DBS's are too weak to be fitted properly, and we therefore use the q_z intercept of the constructed ellipse. Good agreement was found between the two methods. The resulting q_z positions were converted to D_{lam}^{par} values using Eq. 1. For the perpendicular oriented lamellae, the positions of the peaks in the profiles shown in Figure 5.8b together with Eq. 2 were used to determine D_{lam}^{perp}. For simplicity, we use the term D_{lam} throughout, also in the disordered state after 13.5 min, where the value rather corresponds to the size of the correlation hole [37]. During the initial 13.5 min, D_{lam}^{par} and D_{lam}^{perp} show very different behavior as a function of treatment time (Figure 5.9a): During the first 5.3 min, D_{lam}^{perp} is unchanged at 188 Å. Then, D_{lam}^{perp} increases with a rate of 3.5 Å/min, i.e. by 1.9 %/min, and reaches 197 Å after 6.5 min. Thereafter, the value stays constant. In contrast, the behavior of the parallel lamellae is more complex: During the first 2 min, D_{lam}^{par} = 180 Å, i.e. it is smaller than D_{lam}^{perp}. After 2 min, D_{lam}^{par} increases with a rate of 9.5 Å/min, i.e. by 5.3 %/min, and reaches a plateau at 214 ± 5 Å after 6 min. The rate of swelling is thus higher than for the perpendicular lamellae. Then, D_{lam}^{par} decreases until it reaches 201 Å after 13.5 min. After this time, both values stay constant and are very similar to each other.

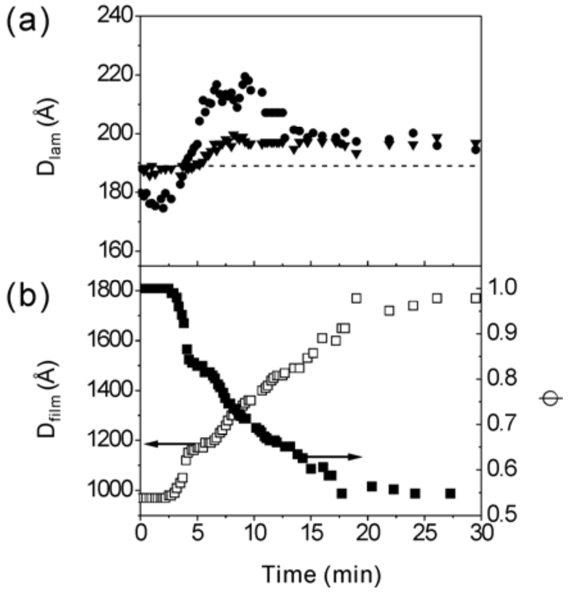

Figure 5.9 (a) D_{lam}^{par} (filled circles) and D_{lam}^{perp} (filled triangles) as a function of treatment time. The dashed line marks the bulk lamellar thickness [31]. (b) Film thickness as a function of treatment time (open squares, left axis) and the resulting volume fraction ϕ of P(S-*b*-B) in the swollen film (filled squares, right axis) as determined from the period of the waveguide oscillations in the GISAXS images.

We conclude that both D_{lam}^{par} and D_{lam}^{perp} change during treatment with CHX vapor. Perpendicular lamellae are much more constrained laterally, and maybe this explains their slower thickness increase. The two types of lamellae differ in behavior during the first 15 min but then reach the same new equilibrium value. In the disordered state after 15 min, there is no more distinction between the two directions. We now relate the swelling behavior of the lamellae to the changes of the entire film, i.e. the overall solvent uptake.

5.3.2.2 Film thickness

The film thickness as a function of vapor treatment time is determined from the period of the oscillations in the DDSR. The resulting film thickness, D_{film}, stays constant at 970 Å during the first 2 min (Figure 5.9b). Then, the film starts to swell at a rate of 42 Å/min, i.e. by 4.3 %/min, until a new equilibrium value at 1780 Å is reached after 20 min. The rate of swelling is lower than the one of the parallel lamellae, i.e., the behavior is non-affine. The final film thickness is 84% higher than in the dry state. The time-dependent volume fraction of polymer, $\phi = D_{film}^{dry} \big/ D_{film}$, decreases from unity to 0.55 in the fully swollen state (Figure 5.9b).

5.3.2.3 Domain sizes

To characterize the average domain sizes of the randomly oriented lamellae, we have determined the FWHMs of the upper DDSR ellipse (P) along q_y (Figures 5.8b and 5.10). During the first 7.5 min, the FWHMs of the DDSR's do not change significantly. Then, they decrease by a factor of ~2.8, and after 13.7 min, they increase rapidly and reach a constant value. The domain sizes of the perpendicular lamellae thus show a transient maximum.

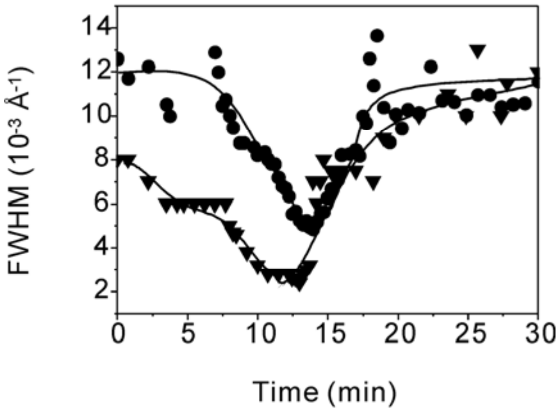

Figure 5.10 FWHMs of the DDSR's (P1) (filled triangles) and the DBS's (P1) (filled circles) as deduced from the peaks in Figure 5.8 The lines are the guides to the eye.

The FWHMs of the DBS along q_z reflect the average height of the correlated stack of parallel lamellae [71]. As shown in Figure 5.10, the domain sizes are similar to those along q_y and show the same behavior, i.e. the domains consisting of parallel lamellae transiently contain a higher number of stacked lamellae. The minima in both domain sizes indicates a transient state of increased long-range order with domain sizes increased by a factor higher than 2.

5.3.3 Maximum film swelling

After 30 min of vapor treatment, the film appeared quasi-static, and we performed a XRR measurement in-situ for comparison (Figure 5.2). We found that the film thickness had increased to 1530 Å with a roughness of 20 Å from initially 1016 Å with a roughness of 10 Å, i.e. the film thickness had increased by 50% due to solvent uptake. The polymer volume fraction, $\phi = D_{film}^{dry} \big/ D_{film}$, has thus decreased to 0.66 ± 0.01. Using GISAXS, we determined the value 0.55 ± 0.02 from fitting the wave guide peaks in the Yoneda band. The difference in film thickness determined by XRR and GISAXS may be due to the difference in illuminated film area (different length of footprint). In the fully swollen state, at the film surface and at the film/substrate interface, indications of layering are observed with PB/CHX being preferentially adsorbed at both surfaces. The remainder of the film is homogeneous with an SLD of 8.35×10^{-6} Å^{-2} which is complies with the volume weighted average of PS, PB and CHX (9.60×10^{-6} Å^{-2}, 8.35×10^{-6} Å^{-2} and 7.56×10^{-6} Å^{-2} for PS, PB and the solvent respectively).

5.4 Discussion

Several interesting effects have been identified during swelling of the thin film with initially mixed lamellar orientation upon treatment with cyclohexane, a slightly PB selective solvent: (i) Vapor treatment improves the long-range order, the increased order, however, is lost again resulting in a final disordered state. (ii) The swelling behavior of the parallel and the randomly oriented lamellae is different: Whereas the behavior of D_{lam}^{par} is characterized by an overshoot of 19 % and a final value which is 12 % higher than the one in the dry state, D_{lam}^{perp} increases after an incubation time of 5 min to the same final value without an overshoot. (iii) Comparison of D_{lam}^{par} and D_{film} shows that additional parallel lamellae are formed. For instance, after 13 min of treatment (just before the film disorders), D_{film} / D_{lam}^{par} = 7.4, which is significantly higher than in the dry state (5.4). This behavior is consistent with our previous observations on a lamellar P(S-*b*-B) film with initially parallel lamellae and treated with toluene.[71] (iv) The transient maxima of the domain sizes of the domains consisting of parallel and perpendicular lamellae reflect the transient state of improved long-range order before crossing the order-to-disorder transition. We will discuss these observations considering the effects of the uptake of CHX on P(S-*b*-B).

The uptake of CHX is expected to have several effects on the P(S-*b*-B) film: (i) The effective glass transition temperature T_g of the polymer blocks is decreased, which is especially important for the PS domain (the T_g of PB is far below room temperature). As the PS glass transition is reached, the copolymer mobility increases, which enables large-scale structural rearrangements. (ii) The effective Flory-Huggins segment-segment interaction parameter between the two blocks, χ_{eff}, is reduced, thus the enthalpic penalty for the creation of additional lamellar interfaces is decreased. (iii) In the presence of solvent, the copolymers assume more coiled molecular conformations than in the dry state where they are stretched away from the interface.[19, 71, 72] This implies an increased demand of interfacial area of each copolymer, thus promoting the formation of additional lamellae. In the following, we will discuss the resulting effect on the film structure.

5.4.1 Decrease of the effective T_g

Following the Equation 3.5, the glass transition temperature T_g of a PS/CHX mixture in bulk varies with ϕ as

$$T_{g,PS-CHX} = \frac{(1-\phi)\alpha_{CHX}T_{g,CHX} + \phi\alpha_{PS}T_{g,PS}}{(1-\phi)\alpha_{CHX} + \phi\alpha_{PS}} \tag{5.1}$$

where α is the cubical thermal expansion coefficient of the fractional free volume, $\alpha_{CHX} = 1.23\times10^{-3}K^{-1}$ [73], $\alpha_{PS} \approx 1.9\times10^{-4}K^{-1}$ [70], and $T_{g,CHX} = 186K$ [74]. To estimate the variation of T_g, we assume for simplicity that CHX is equally distributed in PS and PB. This assumption of equal distribution thus only holds strictly for the later stages when the difference in $\chi_{\text{PS-CHX}}$ and $\chi_{\text{PB-CHX}}$ is small, whereas in the beginning of the treatment, CHX is slightly more PB selective as discussed above. The resulting $T_{g,\text{PS-CHX}}$ values during vapor treatment are given as a function of treatment time in Figure 5.11a. Already after 3.5 min of vapor treatment, $T_{g,\text{PS-CHX}}$ falls below room temperature. We expect the true glass transition at slightly later time than this estimate because CHX is not distributed evenly in the PS and PB domains, but in equilibrium PB is enriched in CHX.

The strong increase of the copolymer mobility thus promotes the feasibility of structural rearrangements after a few minutes of vapor treatment.

5.4.2 Decrease of χ_{eff}

The presence of solvent in the microphase-separated, lamellar morphology not only decreases T_g but also screens the repulsive interaction between the PS and the PB domains. In the absence of solvent, $\chi N = 20$, the diblock copolymer melt is thus in the intermediate-segregation regime [43]. Starting from this low value, it is probable that χN reaches the value of 10.5 upon solvent uptake, where the order-to-disorder transition (ODT) is expected. For a non-selective solvent, χN of the copolymer is replaced by $\chi_{eff}N$ with $\chi_{eff} = \phi\chi$ [75]. Using this assumption in spite of the slight selectivity of CHX, we find that $\chi_{eff}N$ of P(S-*b*-B) decreases with time as shown in Figure 5.11b during treatment with CHX vapor. After a treatment time of ~20 min, $\chi_{eff}N$ has decreased to 11.0, i.e. $(\chi N)_{ODT}$ is reached. Again, this time is only a crude estimate, because the solvent distribution is presumably not equal in the PS and PB domain and because the exact value of $(\chi N)_{ODT}$ may be higher than 10.5 for a low molar mass copolymer, as stated by

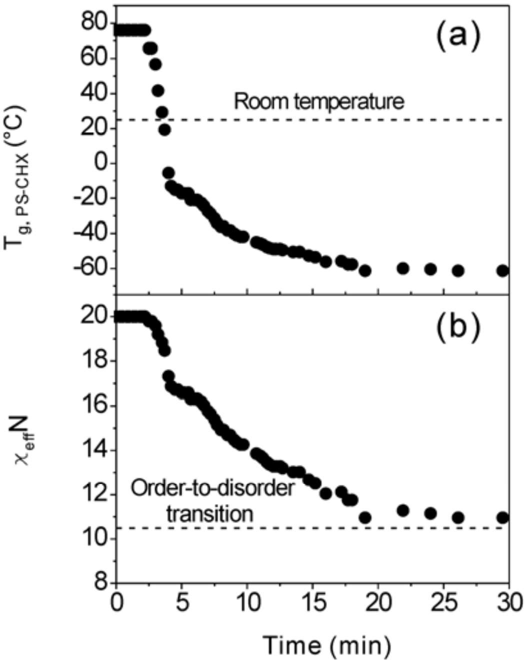

Figure 5.11 Effective T_g (a) and $\chi_{eff}N$ (b) as a function of treatment time. The horizontal dashed lines in (a) and (b) indicate room temperature (25°C) and the order-to-disorder transition.

fluctuation theory [76]. However, it is striking that the ODT is reached significantly later than the glass transition. We assign the vanishing of the DBS's and DDSR's after 13.5 and 15 min, respectively, to the ODT of the copolymer in the presence of solvent.

The transient state of increased lamellar order which persists in the time range 7.5 min to 15 min is thus a result of the competition between the increased polymer mobility facilitating structural rearrangements and the order-to-disorder transition due to screening of the repulsive interaction between PS and PB. Conserving the structure of the vapor-swollen film, e.g. by quick drying or chemical cross-linking, must be carried out during this transient state.

5.4.3 Increase of the degree of coiling

The behavior of thickness of the parallel lamellae – overshoot and leveling-off – resembles very much the one observed in our previous study where the initial morphology was purely parallel and a non-selective solvent, toluene, was used [71]. However, the kinetics is different: In toluene vapor, the maximum of the overshoot was already reached after 3-4 min of treatment. The overshoot was attributed to predominantly uniaxial swelling with an unchanged interfacial area per chain in the first instant and the subsequent deswelling of the lamellae when the copolymers adopt a more coiled molecular conformation. The latter process only becomes possible when the polymers become mobile. It results in undulations of the lamellar interfaces and the creation of additional lamellae to allow more interfacial area per chain.

In the present work, we were able to compare the behavior of the parallel lamellae quantitatively to the mean-field predictions for the behavior of the lamellar thickness as presented in Ref.[77].

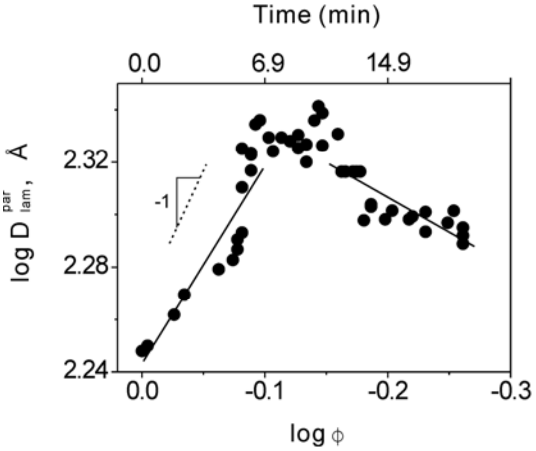

Figure 5.12 D_{lam}^{par} as a function of ϕ (lower axis) in a double-logarithmic representation. The time of vapor treatment is given on the top axis. The lines are fits of power laws, see text. The dashed line marks the predicted behavior $D_{lam}^{par} \propto \phi^{-1}$.

Figure 5.12 shows the dependence of D_{lam}^{par} on ϕ. During vapor treatment, ϕ decreases from 1 in the dry state to ~0.55 in the fully swollen state. In spite of the scatter in the data, two limiting regimes can be discerned: In the high-concentration regime (early times), an increase of D_{lam}^{par} following $D_{lam}^{par} \propto \phi^{-0.76\pm0.11}$ is observed. The swelling is slightly slower than the uniaxial swelling predicted by mean-field theory, $D_{lam}^{par} \propto \phi^{-1}$, for the case that the interfacial area per chain is unchanged from the dry state [77]. The discrepancy may be due to the presence of randomly oriented lamellae. However, this swelling only lasts until $\phi = 0.81$ is reached, i.e. after ~6 min, when D_{lam}^{par} levels off. The glass transition of PS is reached, and the polymer becomes significantly more mobile, which enables the coiling of the copolymers and the formation of additional lamellae. In the low-concentration regime for $\phi < 0.72$, i.e. after ~8 min, $D_{lam}^{par} \propto \phi^{0.27\pm0.04}$. The latter behavior is in agreement with the mean-field prediction $D_{lam}^{par} \propto \phi^{1/3}$ (Ref.[77]) and is related to the higher degree of molecular coiling in the presence of solvent.

This coiling is only possible when the polymers are sufficiently mobile to move along and across the lamellar interfaces.

5.4.4 Behavior of randomly oriented lamellae

The thickness of the perpendicular part of the randomly oriented lamellae stays constant during the first ~5.5 min, presumably because of the strong lateral constraints. Only after this time, the polymer is mobile enough for an increase of D_{lam}^{perp}. Eventually, D_{lam}^{perp} reaches the same value as the D_{lam}^{par}, consistent with a new equilibrium state, the disordered state, as argued above, has been reached at a polymer volume fraction of 0.55 in saturated CHX vapor. An ellipse was found to match the DDSR's well thoughout the vapor treatment. We thus conclude that the lamellae with intermediate orientation follow a behavior intermediate between the parallel and perpendicular ones.

5.5 Conclusion

Solvent vapor treatment offers an efficient route to control the structures in thin block copolymer films, however, the mechanisms are complex. In this study, we report on the structural changes of a lamellar film which features a distribution of lamellar orientations before treatment. We observe that the orientation becomes more well-defined for a certain time, but then the film becomes disordered. Additional parallel lamellae are created during the process, which is consistent with our previous observation that the parallel orientation is the equilibrium one [65, 67]. We relate the changes to the influence of solvent vapor on T_g, χN and the tendency to increased molecular coiling in the presence of solvent.

The time scale of the structural changes (< 30 min) is much lower than what has been reported in the literature for poly(styrene-*b*-methyl methacrylate) having a molar mass of 263 kg/mol [14]. Structural changes have been reported to occur during 120 h of treatment. The reason may be the higher molar mass of the polymer and that the driving force of this system is mainly the change in surface energy by the solvent, whereas, in our case, the film is thicker and the structural changes reflect rather the thermodynamics of the copolymer.

Using a thin film with several lamellae stacked allowed us to separate structural changes along the lamellar normal and within the plane of the lamellar interface, because of the macroscopic orientation of the lamellae along the film surface. Moreover, the vapor treatment of a thin film enabled us to address the low solvent concentration regime which is difficult with bulk samples. We were able to show that lamellar thin films of P(S-*b*-B) qualitatively follow the mean-field predictions at very low solvent concentration, $D_{lam}^{par} \propto \phi^{-0.76\pm0.11}$, whereas they quantitatively follow the predictions at higher solvent concentration, $D_{lam}^{par} \propto \phi^{0.27\pm0.04}$.

However, in this study, ϕ changes with time so D_{lam}^{par} is not only a function of ϕ but also a function of time. Therefore, the structure we observed probably doesn't refer to the equilibrium or stable state for each ϕ. To make it strict, in the next chapter, we carried out stepwise vapor treatment and thus the D_{lam}^{par} is obtained as a function of ϕ and is independent of time.

Chapter 6

Stepwise vapor treatment

6.1 Idea

In the previous chapter, the vapor treatment was performed under saturated CHX atmosphere. A transient state with improved long-range order was observed and the sample became disordered at last. We attribute this phenomenon to the fact that the $\chi_{eff}N$ at the final state is smaller than $(\chi N)_{ODT}$. We suppose that under a proper vapor pressure, a stable state with improved long-range order will appear in the solvent vapor atmosphere.

Therefore, in this chapter, we started the vapor treatment with a much lower CHX vapor pressure and wait until the sample structure was constant with time. Then the vapor pressure was increased slightly, and again we waited until the sample structure was constant with time. In this manner, the sample is stepwise swollen by all together 5 steps. We will see whether there are stable states with improved long-range order in these steps/vapor pressures. Further more, the lamellar thickness was obtained as a function of ϕ but independent with time. Thus the condition of the mean-field theory is fulfilled more strictly.

6.2 Experimental

The polymer used in this study is the block copolymer SB12 (see § 4.1). In-situ GISAXS measurement was performed at Beamline D1, CHESS. The beam was 0.1 mm high and 0.5 mm wide. The wave length was 1.23 Å and the sample detector distance was 1760 mm. The incidence angle used during vapor treatment was $\alpha_i = 0.14$ °, which was larger than the critical angle of the polymer (0.12°) but smaller than the critical angle of Si (0.176 °). Thus the inner structure of the thin film can be determined with a time resolution of only a few seconds. The sample cell used for in-situ stepwise vapor treatment is shown in Figure 6.1. It is similar to the one used for saturated vapor treatment (Chapter 5) but with additional helium gas flow and a white light interferometer. The helium flow was used to dilute the CHX vapor inside the cell. The magnitude of the helium flow was controlled by an adjustable flow meter from 0 to 400 sccm (Standard Cubic Centimeters per Minute). A white light interferometer was fixed at the top of the sample cell to measure the film thickness every 1 s through a glass window.

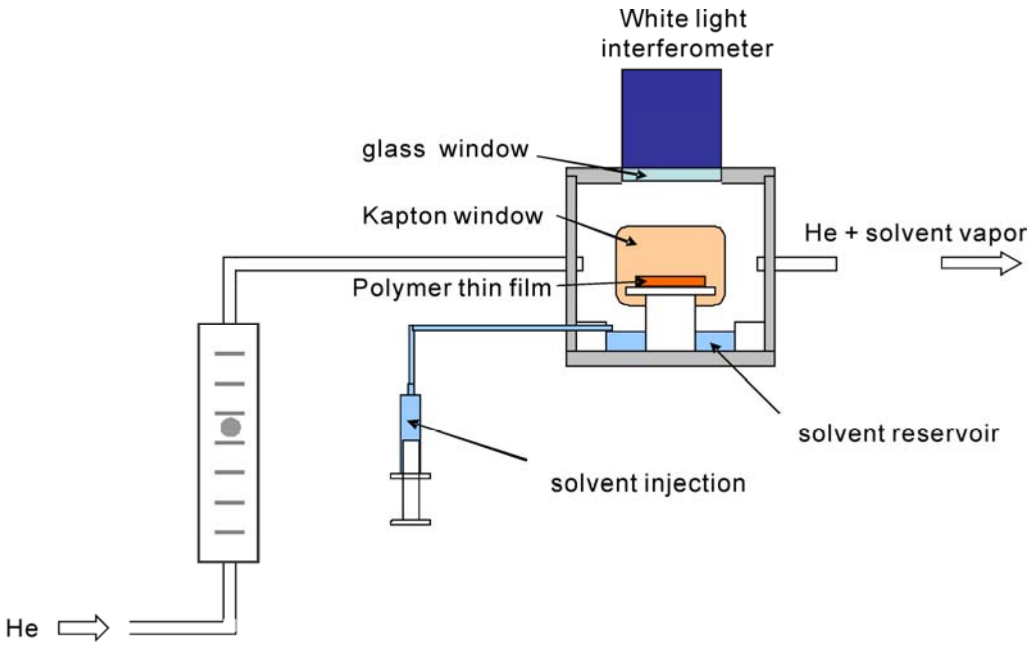

Figure 6.1 Sketch of the sample cell used for stepwise vapor treatment. The X-ray beam enters and exits the cell through the thin kapton windows. CHX solvent can be injected remotely into a reservoir below the sample. A helium flow, which can be adjusted from outside the hutch from 0 to 400 sccm, is connected to the sample cell to dilute the solvent vapor pressure. A white light interferometer is fixed at the top of sample cell to measure the film thickness every 1 s through a glass window.

A time series was initiated such that GISAXS images were taken continuously every 7 s with a helium flow of 92 sccm. After 3 ~ 5 initial GISAXS images were taken, the CHX was injected into the cell while keeping the same helium flow and the same GISAXS image taking rate. This rate was decreased to 37 s per image after 5.5 min of the CHX' injection because the changes in the GISAXS images became slow. This lasted for another 22 min until the white light interferometer showed a constant film thickness and the rearrangement of the polymer chains have finished i.e. no further changes of the GISAXS images. Then the helium flow was decreased to 70 sccm such that a higher CHX vapor pressure was reached. To catch the fast dynamics, the GISAXS image taken rate was set back to 7 s per image for the first 5.8 min and 37 s per image afterwards. It lasted for 24 min until the film thickness became constant and no changes were observable from the GISAXS images. Then the helium flow was further decreased in steps to 44.5 sccm, 37 sccm and 31 sccm respectively. For each step, the GISAXS images were taken every 7 s for the first few minutes and every 37 s afterwards. In each step (except the last one), we waited long enough until no time dependent was observable. The whole stepwise swelling can be seen from Figure 6.2.

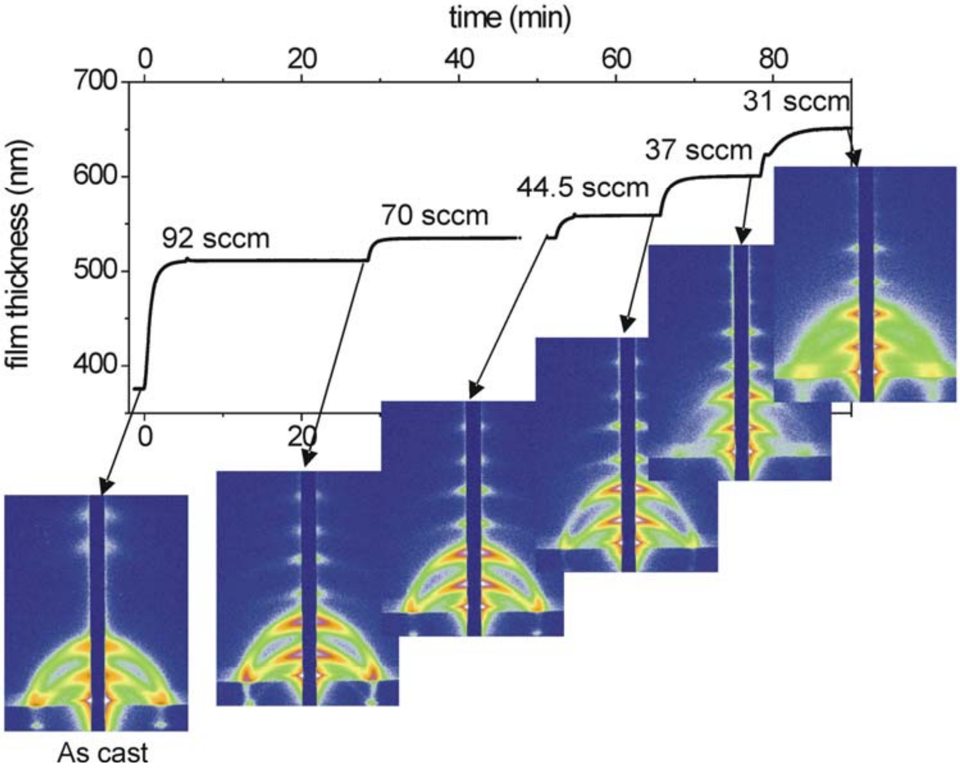

Figure 6.2 Film thickness of P(S-*b*-B) thin film during stepwise swelling. The numbers on the curve indicate the helium flow used to dilute the CHX vapor. The typical GISAXS images after the sample being stable in each step of swelling is given below the curve.

As shown in Figure 6.2, the thin film was swelled in five steps. In each step we waited for 10 ~ 25 min, so that the structural rearrangements were finished (except the last step. For the last step, we did not wait long enough. When we stop the measurement, the D_{lam} was still decreasing). The typical GISAXS images after the swelling and structural arrangement in each step were given below the swelling curve. We first discuss the film structure in the dry state and then we will focus on the details of the structural changes during the first swelling step. Last, we will discuss the lamellae swelling as a function of the volume fraction of polymer, ϕ for all the five steps.

6.3 Results and discussion

6.3.1 Structure of the as-prepared film

Figure 6.3 shows the 2D GISAXS image and its intensity profile along q_z axis of the as-prepared thin film. It shows similar DDSR's as shown in Figure 5.3 in Chapter 5 but with additional 3rd order of DBS's. The appearance of the 3rd order of DBS's indicates that fairly long-range ordered, microphase-separated morphology is present in the film, i.e. lamellae have a dominant distribution of orientation parallel to the film surface. The appearance of the DDSR's also indicates that a small fraction of lamellae are randomly oriented.

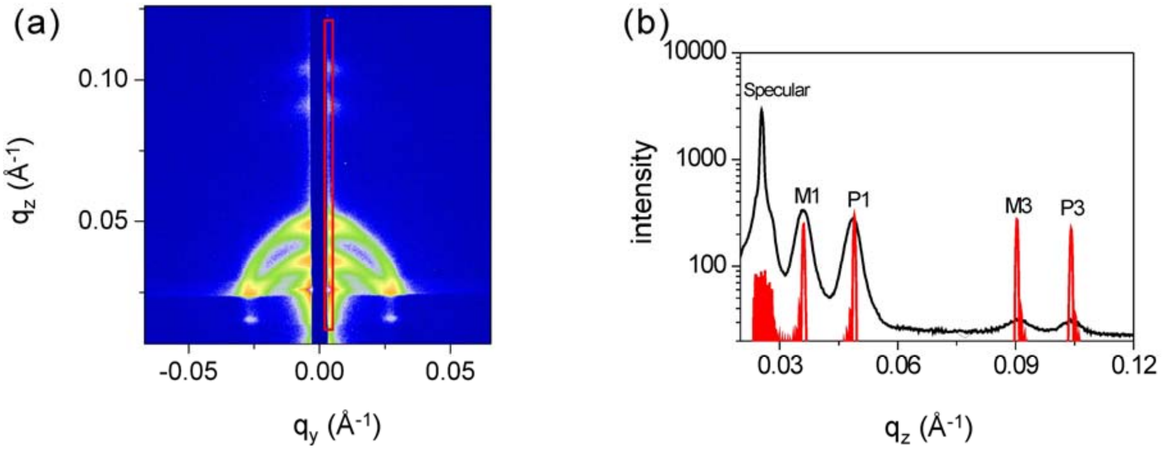

Figure 6.3 2D GISAXS image of the as-prepared sample at α_i = 0.14°(a) and its intensity profile along q_z axis (black curve) together with the peak position fitting (red curve) using *Layers* (§4.4.3.3) (b). The red box in (a) indicates the region of integration used for obtaining the profile in (b) and Figure 6.5.

In Figure 6.3 only the 1st and 3rd order of DBS's are seen because the sample is a symmetric block copolymer, i. e. the volume fraction of the PB domain is 0.49±0.01. Thus the even orders of DBS's are vanished and only the odd orders of DBS's can be observed [65]. The lamellar thickness and the incidence angle can be determined from the positions of DBS's by fitting with program *Layers* (see §4.4.3.3). From the fitting, a lamellar thickness of 22.5 nm and an incidence angle of 0.142° are obtained. The fitted incidence angle 0.142° is well in accordance with the motor set value 0.14°. The film thickness of the as-prepared sample is measured directly by the white light interferometer with a value of 375.5 nm.

We conclude that, in the dry state, the film consists of fairly long-range ordered lamellae with a domain orientation parallel to the film surface. In contrast, in Chapter 5, the P(S-*b*-B) diblock copolymer having a film thickness of ~ 100 nm shows a lamellar structure with a broad distribution of lamellar orientations. The main reason is that the UV treated Si wafer is not favorable for parallel lamellae orientation. Here we use the same substrate but the film is much thicker (375 nm). The increase of the film thickness weakens the influence of the substrate so that lamellae with a dominant distribution of orientation parallel to the film surface are observed.

6.3.2 The first step of swelling

After several initial GISAXS images were taken with the helium flow of 92 sccm, CHX solvent was injected into the sample cell while keeping the helium flow at the same level. Drastic changes of the GISAXS images were observed (Figure 6.4): (i) During the first ~3 min, the 3rd order of DBS's weakened and disappeared. (ii) New DBS's in between the 1st and 3rd order of DBS's appeared from after ~40 s. (iii) The overall scattering intensity increased. (iv) The GISAXS images became stable with 6 DBS's after ~10 min.

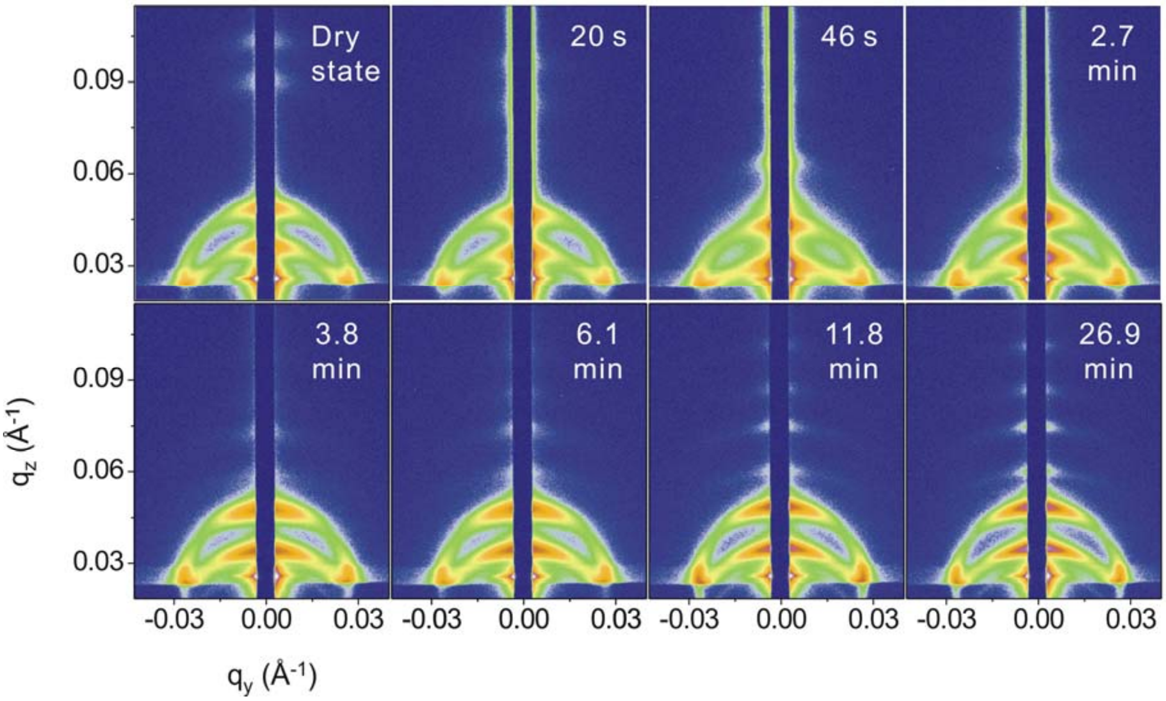

Figure 6.4 GISAXS images of the film during treatment with diluted CHX vapor (the first step in Figure 6.2) for the time given in the figures. The helium flow is 92 sccm. $\alpha_i = 0.142°$. The logarithmic intensity scale runs from 15 to 5000 cts for all images.

The observations are more clearly seen in the intensity profiles through the DBS's (Figure 6.5): At the very beginning (dry state), 4 Bragg peaks besides the specularly reflected peak can be seen, 2 of 1st order, M1 and P1 and 2 of 3rd order, M3 and P3 (Figure 6.3b). When injecting CHX, the peaks changed dramatically and in a complex manner for the first few minutes: M3, P3 first weakened and then disappeared and then new peaks grew. After ~10 min, 6 peaks besides the specularly reflected peak can be seen remaining unchanged with time. The whole swelling process can thus be divided into two regimes i.e. the transition regime (the first few minutes) and the final, stable state regime (after ~10 min). In the following we will discuss the two regimes separately. Since in the transition regime, the DBS's changed dramatically and in a complex manner, we will start first with the more clear stable states.

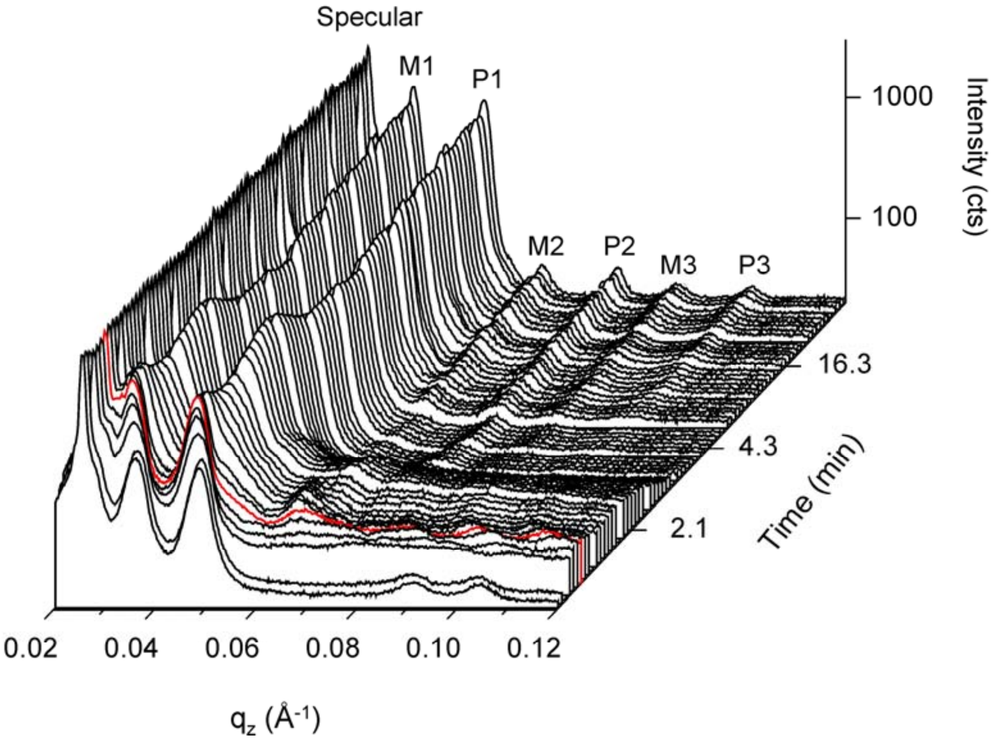

Figure 6.5 Intensity profiles along q_z, i.e. through the DBS's from the GISAXS images (partially shown in Figure 6.4) as a function of treatment time: From the dry states until end of the first-step swelling (~30 min). The red curve is corresponding to 40 second of vapor treatment.

6.3.2.1 Stable states

Six DBS's were seen in the stable state (stabilized swollen state). To identify the DBS's, the intensity profiles were fitted with *Layers*. The fitting of the dry state intensity profile has been done in Figure 6.3b very successfully. It is a good starting point for the new fitting. In Figure

6.6a we use the same fitting parameters as for the dry state except a slightly larger lamellar thickness. With a lamellar thickness of 23.3 nm and an incidence angle of 0.142°, 4 peaks can be well fitted. Thus the 1st order DBS's M1 and P1 and the 3rd order DBS's M3 and P3 are indentified, whereas two peaks between the P1 and M3 can not be fitted. Previously, we have mentioned that, for symmetric block copolymers, only the odd order of DBS's can be seen. So in the fitting we always set the thickness of PS layers exactly equal to that of the PB layers. However, CHX is slightly PB selective. In the swollen state the PS and PB domains are not symmetric any more. Therefore we set the thickness of PB layers slightly larger than that of PS layers, i.e. the volume fraction of PB is 0.6. This way all the six peaks can be fitted with the same lamellar thickness and incidence angle (Figure 6.6b). Therefore, all the six peaks are indentified.

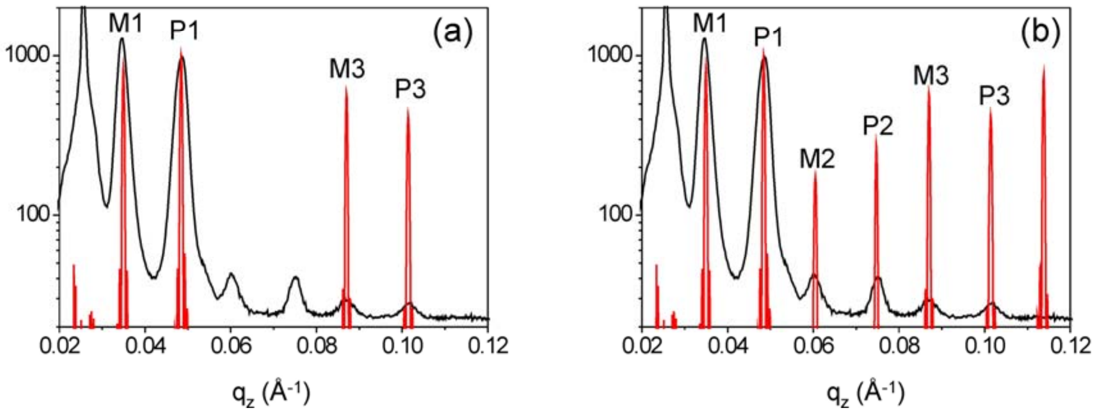

Figure 6.6 Intensity profile along q_z from the last GISAXS image of Figure 6.4 together with the fittings assuming that the block copolymer is symmetrical (a) or asymmetrical (b)

Each peak can also be fitted with a Gaussian function, thus the peak width is obtained. It is interesting to compare the peak width with the one from the dry state. From table 6-1 we see that after the sample has become stable in the first-step swelling, all the DBS's become much sharper than in the dry state.

Table 6-1 The FWHMs of the 1st and 3rd order peaks from Figure 6.3b and 6.6

	M1 (Å^{-1})	P1 (Å^{-1})	M3 (Å^{-1})	P3 (Å^{-1})
Dry state	0.0042	0.0039	0.0053	0.0059
Swollen state	0.0025	0.0029	0.0039	0.0036

We conclude that when the sample is stable in the first-step swelling, the lamellar thickness increases from 22.5 nm to 23.3 nm, and the appearance of the 2nd order of DBS's is consistent with the slight selectivity of the CHX to PB. The sharper and more intensive DBS's in swollen state also indicate that the vapor annealing in the described conditions improves the lamellar phase-separation i.e. increases long-range order.

6.3.2.2 The transition process

The transition process lasted for a few minutes from the start of the vapor treatment until the stable state was reached. From the above study we have learned that in the dry state the 1st and 3rd order of DBS's were seen but at the stable state not only the odd order but also the 2nd order of DBS's were seen. However in the transition regime the behavior of the DBS's was very complex. From Figure 6.5 we can see the 1st order DBS's remained rather stable in this regime with some position shift corresponding to the variation of the lamellar thickness. But the 3rd order DBS's disappeared shortly after the injection of the CHX solvent and appeared again ~40 s (red curve in Figure 6.5), but they only lasted for a few second and lost again. They appeared again only when the stable state was reached. Meanwhile, the 2nd order DBS's appeared around 40 s (M2) and around 3.3 min (P2) and remained with small position shifts.

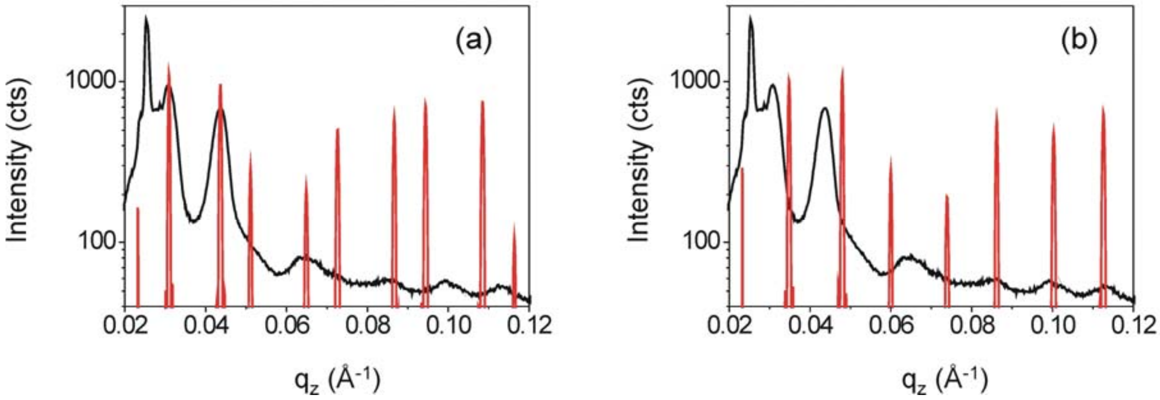

Figure 6.7 Intensity profile along q_z together with the fits using program *Layers*. For the fitting, $\alpha_i = 0.142°$, volume fraction of PB, $f_{PB} = 0.58$ (to get the even order), and the lamellar thickness, $D_{lam} = 28.5$ nm for (a) and $D_{lam} = 23.6$ nm for (b).

Since many DBS's appeared at 40 s, it is interesting to fit the intensity profile at this time. However, unlike in the dry state or in the stable state, it is impossible to fit all the peaks in this intensity profile with a single value of D_{lam} (Figure 6.7). When the positions of DBS's at low-q_z

are fitted, the ones at high-q_z are dismatched (Figure 6.7a) and vice versa (Figure 6.7b). The resulting D_{lam} from fitting the position of DBS's at low and high-q_z are 28.5 nm and 23.6 nm respectively. Both values are larger than the one in the stable state. This complex D_{lam} behavior will be further discussed in the next section. Now we concentrate on the dismatch of the fitting.

What causes the failure of the peak position fitting? It works successfully in the dry state and the stable state. Nevertheless, it is clear that, the model used for the calculation cannot reflect the real structure at this special swelling moment. One possible reason is that the lamellar structure has changed to some other structure such as cylinder due to the increase of the f_{PB}. All of the previous calculations are based on lamellar structure. If the lamellar micro-phase separation transformed to cylindrical micro-phase separation, the calculated peak position cannot fit. However, from Figure 6.7a, besides the specularly reflected peak, the first 6 calculated peaks fit the experimental data. It is impossible that the sample consists of other structure, otherwise it won't fit so many peaks. Furthermore, if the micro-phase diagram has transformed to cylinder, higher order of DBR's should be seen due to regular lateral structure [78]. The remained possible reason is that the film swelling is uneven i.e. the lamellar thickness differs from the top to the bottom of the thin film. This explains the lamellar thickness (28.5 nm) obtained from fitting the DBS's in low-q_z is larger than that in high-q_z (23.6 nm). We learned from §4.4.3.4 that the low-q_z scattering comes more from the film surface while the high-q_z scattering comes more from the film bottom. It is reasonable that the lamellae at the surface of the thin film swell more than that at the bottom at the beginning of vapor treatment. This uneven swelling explains also the loss of the 3rd order DBS's from ~40 s to ~5 min.

We conclude that in the transition state, an uneven swelling of the lamellae is observed. The lamellae at the top of the thin film swell much faster than that at the bottom. The gradient of the lamellar thickness breaks the 3rd order of the DBS's in the time region from ~40 s to ~5 min.

6.3.2.3 Lamellae swelling

Peak position fittings were done for all curves in Figure 6.5. In dry state and stable states, all the peaks are matched with one D_{lam} while for the curves in transition regime, two D_{lam}'s were deduced and the D_{lam} for the lamellae at surface were used in Figure 6.8. The resulting lamellar thicknesses are plotted as a function of time in Figure 6.8 (red dots) and four interesting phenomena can be seen: (i) At the very beginning, the lamellar thickness increased very rapidly, even faster than the film thickness (blue curve). (ii) A sharp overshot with a swelling of 35%

was seen. The overshot was much sharper than the case in the saturated vapor treatment (Chapter 5). (iii) At 0.6 min, there was a change of the slope (pointed out by the black dashed line in Figure 6.8). (iv) The film thickness leveled off earlier than the lamellar thickness.

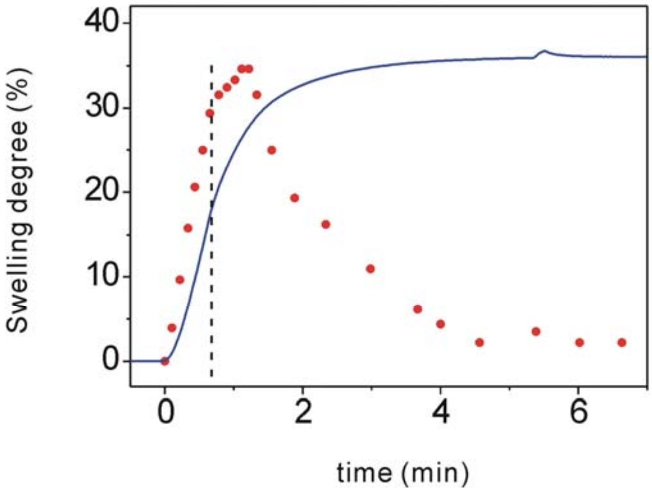

Figure 6.8 The degree of lamellae swelling (red dots) and the degree of thin film swelling (blue curve) as a function of vapor treatment time in the first swelling-step. The perpendicular black dashed line indicates the first inflexion of the lamellae swelling

We would expect that at the very beginning of the swelling, the film thickness is proportional to the lamellar thickness leading a same degree of swelling for both, i.e. in Figure 6.8, the red dots fell on the blue curve at the very beginning (before the first kink). However, we can see from Figure 6.8, it is not in this case. The lamellae swell faster than the whole film. To explain this phenomenon we have to look back how we get the lamellar thickness. We obtained the lamellar thickness by fitting the position of the DBS's. However, because of the uneven swelling, we cannot fit all the DBS's at the beginning of the swelling. Therefore, we only fit the first order of the DBS's. As already discussed before, the lamellae near the surface contribute dominantly to the first order DBS's and they swell faster than the lamellae near the bottom. The film thickness is proportional to the average lamellar thickness and the latter is smaller than the lamellar thickness near/at the film surface.

The fast swelling of the lamellae lasted only a few minutes. Two kinks appeared, one at 0.6 min (indicated by the dashed black line in Figure 6.8) and the other at 1.17 min (the highest point in Figure 6.8). After the first one, the lamellae swelled much more slowly and after the second one, the lamellae started to deswell. It is natural to assume that one of the kinks represents the glass transition of PS. Considering that the rearrangement requires a certain time, especially when the

T_g of PS is not yet far below the ambient temperature. There must be a delay between the glass transition of PS and the decrease of the lamellar thickness. Therefore the kink at 1.17 min (the highest point) cannot be the transition point. However the kink at 0.6 min is a likely candidate: After this turning point, the lamellar thickness still increases but with an obvious smaller speed (Figure 6.8). This can better be discussed when D_{lam} is plotted as a function of ϕ (Figure 6.9).

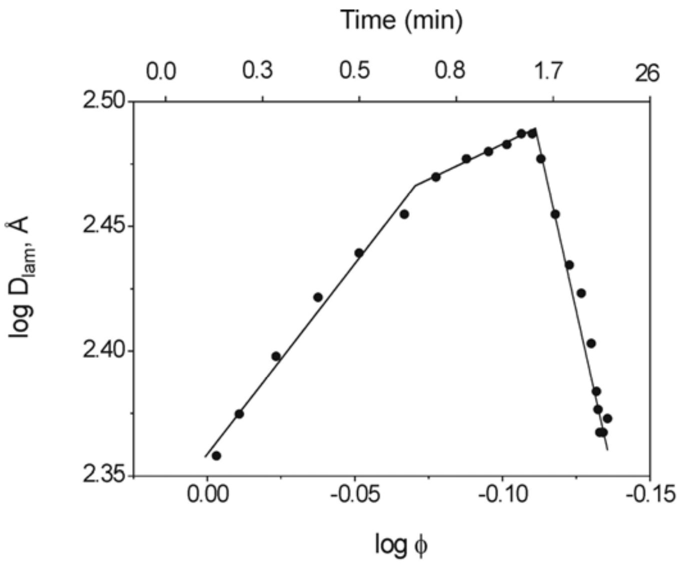

Figure 6.9 D_{lam} as a function of ϕ (lower axis) in a double-logarithmic representation. The time of vapour treatment is given on the top axis. The lines are fits of power laws, see text.

Figure 6.9 shows the dependence of D_{lam} on ϕ. The two kinks can be better seen here. These two kinks are at $\phi = 0.85$ and $\phi = 0.77$ respectively and marked tree regimes: In the high-concentration region ($\phi > 0.85$), an increase of D_{lam} following $D_{lam} \propto \phi^{-1.5\pm0.1}$ is observed. The swelling is faster than the uniaxial swelling predicted by mean-field theory, $D_{lam} \propto \phi^{-1}$, for the reason of uneven swelling at this time region. This swelling lasts until $\phi = 0.85$, i.e. for ~ 0.6 min. Then the swelling speed decreased and an increase of D_{lam} following $D_{lam} \propto \phi^{-0.57\pm0.04}$ is observed. Two possible reasons may explain this much slower swelling. One is the uneven swelling ends at the first kink ($\phi = 0.85$) and the other is that the glass transition of PS is reached here. The ending of uneven swelling is a gradual process and moreover from the GISAXS images it is seen that the DBS's at high-q_z are very similar before and after $\phi = 0.85$ which points out the gradience of Dlam has no obvious change at this point. Therefore, we conclude that the appearance of the first kink come from the glass transition of PS. Since at $\phi = 0.85$ the glass transition of PS is reached and we know from Kelley-Buecher's equation

(Equation 3.5) that for pure PS the glass transition is reached at $\phi_{PS} = 0.93$ (volume fraction of PS), we can then estimate the selectivity of the CHX in our sample. Let's assume that the partial of the CHX entering PS domain is x, the partial entering PB domain is (1-x); both volumes of PS and PB are the same and equal to 0.5. The volume of CHX is then equal to 1-0.85=0.15. We have:

$$\frac{0.5}{0.15x + 0.5} = 0.93$$

Resolving the above equation, we get $x = 0.25$ .Therefore, we conclude that approximately 25% of CHX goes into PS block and the rest goes into the PB domain. It is compatile with the theory predictions [29, 30].

The slow swelling ends at the second kink at $\phi = 0.77$ and the D_{lam} decreases with ϕ following $D_{lam} \propto \phi^{5.28\pm0.00}$. In this low-concentration regime, the effective T_g of PS is significantly lower than the ambient temperature and the polymer becomes significantly more mobile, which enables a very fast rearrangement. However, the mean-field theory predicts a decrease of D_{lam} following $D_{lam} \propto \phi^{1/3}$ which is much smaller than in our case. This may due to the fact that the copolymer is in a nonequilibrium state (highly stretched) before the deswelling. The theory predicts the D_{lam} changes from one equilibrium state to another, instead of from a stretched state to equilibrium state.

The film thickness is the product of the average lamellar thickness and the number of lamellae. The decrease of D_{lam} together with the increase of D_{film} indicates the formation of additional lamellar layers. The formation of new layers requires large rearrangement of the polymer. During this process, of course, the long-range order of the lamellae will be perturbed and this is observed by the loss of 3rd order DBS's in Figure 6.5, between 2 and 4 min.

6.3.3 Further swelling

6.3.3.1 Nonequilibrium

6.3.3.1.1 Results

After the stable state of the first-swelling had been reached for more than 10 min, the helium flow was decreased to 70 sccm and the second swelling-step began. Since the second step was much smaller than the first one, no uneven swelling was observed. The fitting of the positions of the DBS's revealed that D_{lam} first increased and reached the maximum value of 23.8 nm in ~ 30 seconds and then decreased to 23.3 nm. The decrease lasted roughly 2 min and D_{lam} leveled off afterwards. Meanwhile, the D_{film} increased from 511 nm to 530 nm for the first ~ 2 min and then increased much slower and leveled off with a value of 535 nm.

The 3rd swelling-step started 23 min after the second swelling-step, with a helium flow of 44.5 sccm. The behavior of the D_{lam} was very similar as in the second step: D_{lam} first increased and reached the maximum value in ~ 26 seconds and then decreased slightly and levels off.

The 4th swelling-step started 13 min after the 3rd swelling-step, with a helium flow of 37 sccm. Instead of first swelling, D_{lam} incubated for the first ~ 20 s and then decreased slightly and leveled off.

The 5th swelling-step started 13 min after the 4th swelling-step with a helium flow of 31 sccm. D_{lam} first increased and reached the maximum value of 23.1 nm in 14 seconds, then D_{lam} keeped decreasing afterwards. The 5th swelling-step was measured for 10 min and the D_{film} leveled off at ~6.6 min while D_{lam} kept decreasing until the stop of the measurement.

6.3.3.1.2 Discussion

The unexpected increase of the lamellar thickness points to a nonequilibrium state at the beginning of each swelling step. The nonequilibrium is due to the delay of the rearrangement of the polymer chains, i.e. the polymer needs time to establish equilibration. This phenomenon helps us to estimate the time scale of the rearrangement of polymer. We conclude the polymer needs a few tens of seconds to acquire new equilibration responding to the variation of ϕ. The delay time may differ for different $\Delta\phi$, i.e. the smaller $\Delta\phi$ responding to shorter delay. Moreover, since the decrease of lamellar thickness almost stop at the same time as the stop of film swelling, it implies that the delay of the rearrangement of the polymer occurs dominantly at the beginning. The well-ordered lamellar structure acts as a big hindrance for rearrangement of the polymer chains. The polymer chains have to struggle a lot before they can move through the neighbor layers, but if the rearrangement starts, they can rearrange themselves much faster.

However, it is interesting that the lamellar thickness decreases more and longer at the 5th swelling-step (The D_{lam} was still decreasing when we stopped the measurement). At this step, the polymer chains have the highest mobility and should rearrange themselves fastest i.e. reaches the equilibrium fastest. This raises a question: Do the stable states in the first 4 swelling-steps really reach the equilibrium? We will discuss it in the following session.

6.3.3.2 Scalling law

Figure 6.10 shows the change of D_{lam} as a function of ϕ in a double-logarithmic representation for the whole stepwise swelling. Four linear regions can be seen and in each region a linear fitting is performed. The D_{lam} follows $D_{lam} \propto \phi^{-1.5\pm0.1}$, $D_{lam} \propto \phi^{-0.57\pm0.04}$, $D_{lam} \propto \phi^{5.28\pm0.00}$ and $D_{lam} \propto \phi^{0.14\pm0.03}$ in the high-concentration region ($\phi > 0.85$), in $0.85 > \phi > 0.77$, in $0.77 > \phi > 0.73$ and in the low-concentration region ($\phi < 0.73$), respectively. The first 3 regions ($\phi > 0.73$) occurred in the first step of the swelling and had been discussed in §6.3.2. We conclude that the equilibration is not reached in these regions. In the low-concentration region ($\phi < 0.73$), four black filled circles correspond the stable states under four different CHX vapor pressures. In the stable states, the D_{lam}'s are constant with time. Together with the fact that the sample is far above the glass transition temperature, i.e. the sample is very mobile, it is likely that the sample is in the equilibrium. However, in this region, D_{lam}'s followed $D_{lam} \propto \phi^{0.14\pm0.03}$ and thus a question is raised. We know from the mean-field theory that in the low-concentration region D_{lam} is expected to be proportional to $\phi^{1/3}$ (instead of $\phi^{0.14}$) in equilibration. Further more, the four stable states were reached in 3 or 4 minutes whereas in the 5th swelling-step, the stable state was never reached even after 10 min. It is abnormal because the sample should reach equilibration fastest in the 5th swelling-step. If in the 5th swelling-step the sample can not reach the equilibrium in 10 min, it cannot reach the equilibrium in 3-4 min in the previous four swelling-steps either. Therefore the 4 stable states cannot be equilibrium states. In low-concentration region, the D_{lam} is expected to decrease following $D_{lam} \propto \phi^{1/3}$. However, the decrease of D_{lam} requires the formation of new lamellar layers i.e. large rearrangement. When the sample is well ordered in lamellae, the polymer chains have to travel across existent lamellae to form a new one. However it is impossible if the $\chi_{eff} N \gg (\chi N)_{ODT}$. In this case, the D_{lam} can not decrease freely, thus meta-stable states with larger D_{lam} following

$D_{lam} \propto \phi^{0.14\pm0.03}$ are observed. Therefore, we conclude, the stable states observed are not equilibrium but meta-stable states.

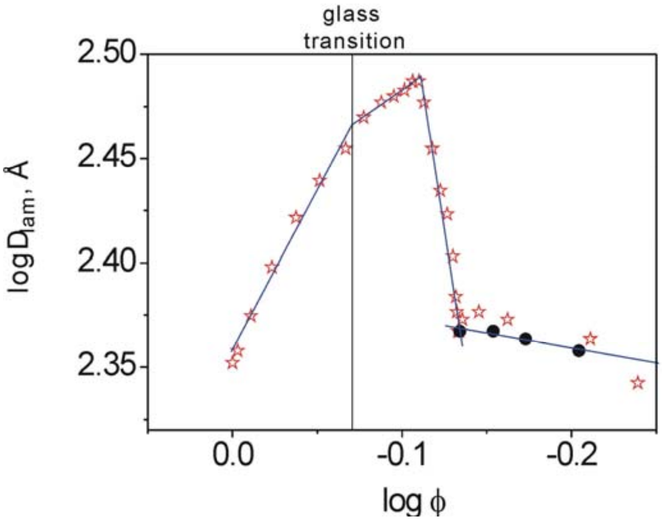

Figure 6.10 D_{lam} as a function of ϕ in a double-logarithmic representation for the whole stepwise swelling. The four black filled circles represent the stabilized state in the 1st to 4th swelling-steps where the red stars represent the lamellar thickness may still change with time. The vertical black line indicates the glass transition of PS and the blue line is the linear fitting. See text

Though not observed directly, we believe that the NOT enough decrease of D_{lam} accumulates the tensions in the sample. When the tension is too big, the metal-stable states collapse and new equilibration may be established. It is similar as what we observed in the first swelling-step i.e. the sudden strong decrease of D_{lam}.

6.4 Conclusion

6.4.1 The first swelling-step

Vapor treatment with a solvent vapor pressure much lower than saturation (with a helium flow of 92 sccm) is proved to be an efficient way to improve the long-range order of lamellae (table 6-1). In this vapor pressure, the thin film is swelled for 36% and the volume fraction of polymer is $\phi = 0.73$. Thus the glass transition of PS is reached and meanwhile $\chi_{eff} N \approx 18$, is above $(\chi N)_{ODT}$. In the dry state only the 1st and 3rd order of DBS's are seen due to the symmetry of the PS and PB domain. However, in fully swollen state, the 2nd order of DBS's appears as well due to the selectivity of CHX for PB resulting in a higher degree of swelling for the PB part of the lamellae. At the very beginning of the vapor treatment, an uneven swelling of the thin film is observed, i.e. the lamellae at the film surface swell faster than those deep in the film. The lamellar thicknesses obtained from the position of the 1st order DBS's are given in Figure 6.8 together with the film thickness as a function of treatment time. Initially, D_{lam} increases rapidly and even faster than the film thickness. This is due to the fact that mainly the upper (more swollen) lamellae contribute to the average position of the 1st order DBS's. The increase of D_{lam} reflects that the uptake of solvent results mainly in swelling along the lamellar normal. After ~0.6 min of treatment, the swelling of the lamellae abruptly slows down. We attribute this slowing down to the glass transition of the PS domain: After having taken up a sufficient amount of CHX, PS goes from the glassy to the liquid state, and the block copolymers become significantly more mobile. The two blocks can now assume more coiled molecular conformations, which are entropically favored when solvent is present [72]. These more coiled conformations result in an increased interfacial area per copolymer and in a lower lamellar thickness than for pure uniaxial swelling along the film normal. After ~1.3 min, suddenly the lamellae start to de-swell strongly. We have observed this effect before [71], and have attributed it to the strongly coiled molecular conformations of the PS and the PB domain. The interfacial demand is now so high that the copolymers cannot be accommodated at a certain lamellar interface any longer. Therefore, additional lamellae are formed, and the blocks can relax to their new (coiled) equilibrium conformation with a lower $\mathrm{D}_{\mathrm{lam}}$ than in the as-prepared state. Eventually, D_{lam} levels off after ~4 min of treatment, i.e. a new equilibrium state is reached. From the kink of the lamellar thickness at 0.6 min, the selectivity of CHX in our sample is estimated that ~25% of CHX goes into PS domain and the rest goes into the PB domain.

6.4.2 The other swelling-step

In the further swelling, at the beginning of each step, a transient state is observed. The transient state is characterized by an overshoot of the lamellar thickness. Then the sample becomes stable after a few minutes except the last step. Though the sample has passed the glass transition, the overshoot of the lamellar thickness reveals that the polymer is still rearranging itself. This rearrangement takes one or two minutes until the sample reaches a stable state. This gives us a clue how fast the polymer can rearrange itself. More interesting, the lamellar thicknesses in the stable states are much larger than predicted ones by the mean-field theory which implies that even the stable states are not equilibrium states. We contribute it to the screening effect of the already existent well-ordered lamellae, which hinder the travelling of polymer chains thus hinder the formation of new lamellae. Therefore a meta-stable state with a more stretched chain conformation is observed.

Chapter 7

Vapor treatment with saturated cyclohexanone

7.1 Idea

We have discussed vapor treatment with slightly PB selective solvent CHX in saturated vapor atmosphere in Chapter 5 and in stepwise-increasing vapor pressure atmosphere in Chapter 6. However, as demonstrated previously, one of the most key effects of the solvent is to make the PS domain soft and mobile. Therefore a PS selective solvent may benefit this purpose. In this Chapter we will discuss vapor treatment with CHXO, which is PS selective and has a 13 *k* lower T_g than that of CHX. Both of the properties help to soft the PS domain. Further more, the vapor pressure of CHXO is very low (3.1 mmHg @21°C). It is only 1/25 of that of CHX. Therefore, even with saturated CHXO vapor, there is no risk that too much solvent might enter the thin film and lead to disorder.

7.2 Setup

The polymer used in this study is the commercial block copolymer SB4908 (see § 4.1). It is spin-cased to an acid-bath cleaned Si substrate (see § 4.1). The in-situ vapor treatment was performed in the beamline BW4, HASYLAB in DESY. The beam was 25 µm high and 48 µm wide. The wave length was 1.381 Å and the sample detector distance was 1972 mm. The incidence angle used during vapor treatment was $\alpha_I = 0.15$ °, which is larger than the critical angle of the polymer (0.12°) but smaller than the critical angle of Si (0.176 °). Thus the inner structure of the thin film can be determined with a time resolution of only a few seconds. The sample cell used for in-situ vapor treatment is the same as described in Chapter 6 (Figure 6.1). However, since the CHXO is oil-like solvent, its saturated vapor pressure is very low, therefore vapor treatment was performed only under saturated vapor atmosphere.

7.3 Result and discussion

We first discuss the film structure in the dry state and then describe the structural changes when the sample is subject to CHX vapor.

7.3.1 Structure of the as-prepared film

The film thickness of the as-prepared thin film measured by the white light interferometer is 203 nm. Figure 7.1 shows a 2D GISAXS image of the as-prepared thin film (measurement time 5 min). It features two orders of DBS's namely M1, P1 and M3, P3 respectively but no DBR's. A long-range ordered lamellar micro-phase morphology with the lamellar orientation parallel to the film surface was thus present in the film.

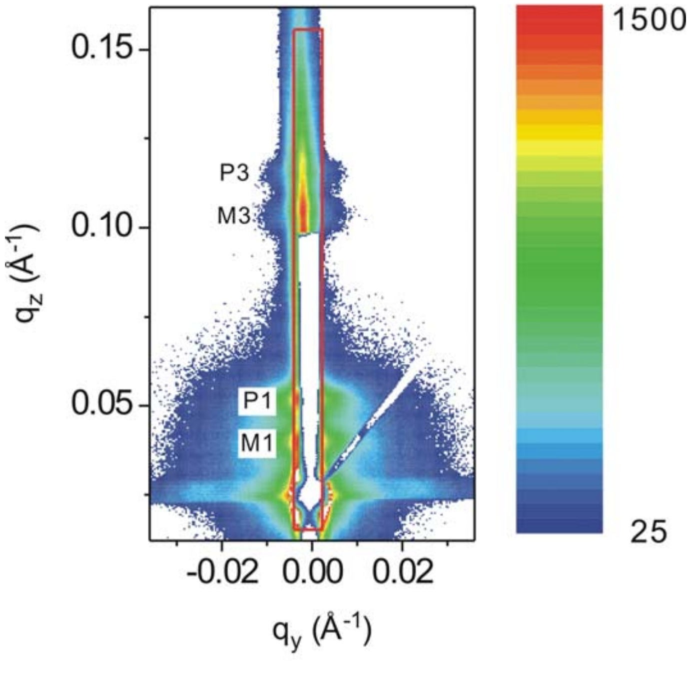

Figure 7.1 2D GISAXS image of the as-prepared sample at $\alpha_i = 0.15°$. The measuring time was 5 min. The DBS's are marked by M1, P1, M3, P3 in the image, respectively. The red box indicates the range of integration for the intensity profile in Figure 7.2. The blank region at $q_y = 0$ comes from a point-like (the lower) and a rod-like (the higher) beamstop.

We have observed in Chapter 5 that SB12, which is very similar as SB4908, has a short-range ordered morphology with randomly oriented lamellae on Si substrate cleaned by UV treatment. In contrast, the present sample was spin-cased onto a Si substrate which was first cleaned by acid bath and then coated with methanol and acetone chronologically. The latter process is to make the substrate hydrophobic. Thus the substrate is selective to PS. and benefit a parallel lamellar orientation.

More details are observed from the intensity profile along q_z axis and its peak position fittings (Figure 7.2). First, not only the 1st and 3rd order of DBS's but also weak 2nd order DBS's were observed. This is due to the asymmetry of the PS and PB domain (however not accordant with the calculated value, $f_{PB} = 0.51$); Second, as shown in the figure, it is impossible to fit all the peak positions with one D_{lam}: When the peak positions of the 1st order DBS's are fitted, resulting in a D_{lam} of 22.2 nm, the 3rd order DBS's are dismatched (Figure 7.2 a) and vice versa resulting in a lamellar thickness of 21.4 nm (Figure 7.2 b). Therefore, we conclude that the lamellar thickness for the as-prepared sample is not constant: the lamellae close to the surface have a thickness of ~ 22.2 nm which is very similar as we observed in Chapter 6 (22.5 nm), meanwhile the lamellae close to the substrate have a smaller thickness of ~ 21.4 nm. We attribute the lamellar thickness decrease close to the substrate to the selectivity of the substrate to PS. In detail, because of the attraction of the substrate to PS, the thickness of the PS layer close to the substrate is smaller than that far away.

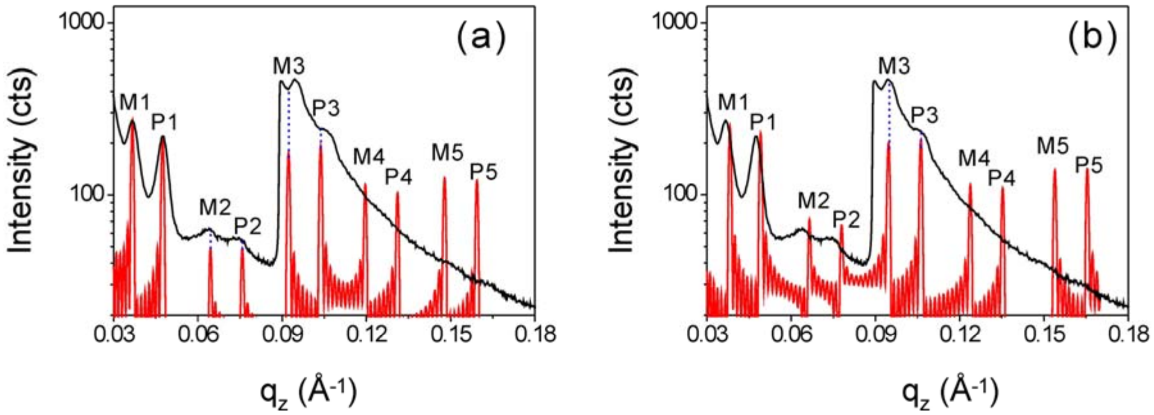

Figure 7.2 Intensity profile along q_z axis of the 2D GISAXS image from Figure 7.1 together with the peak position fittings using *Layers*. Since it is impossible to fit all the peak positions with one D_{lam}, the 1st order peaks are chose to fit in (a) and the 3rd order peaks are chose to fit in (b). Two lamellar thicknesses of 22.2 nm and 21.4 nm are acquired respectively. The intensity increase at $q_z > 0.089$ Å^{-1} is due to the end of the rod-like beamstop.

We conclude that, in the dry state, the film consists of fairly long-range ordered lamellae with an orientation parallel to the film surface; The lamellar thickness differs with depth: the lamellae close to the substrate is smaller than that close to the film surface due to the attraction of the substrate to the polymer.

7.3.2 Structural changes in saturated CHXO vapor

Upon injection of liquid CHXO into the sample cell, the changes of the GISAXS images are observed: (i) In the first a few minutes, only the intensity of the GISAXS image increased rapidly. (ii) After ~ 12 min, side maximums were seen in the DBS's and were moving towards higher q_y with time (Figure 7.3). (iii) Meanwhile, DBS's were prolonged along q_y and bent towards the center of the specularly reflect beam (Figure 7.3). (iv) After ~ 60 min, the intensity of the GISAXS image decreased again (Figure 7.3).

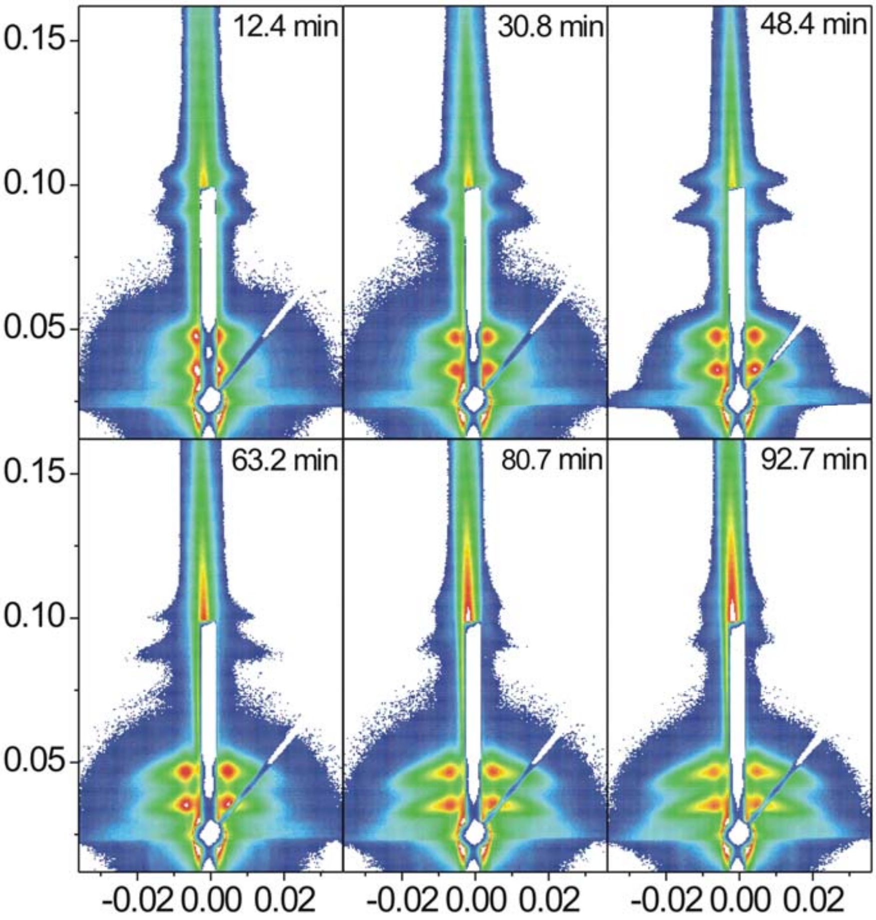

Figure 7.3 GISAXS images of the film during treatment with saturated CHXO vapor for the starting times given in the figure. $\alpha_i = 0.15°$. Each measurement takes 10 min and the logarithmic intensity scale runs from 60 to 9000 cts for all images.

Details will be discussed in the following focusing on the long-range order, lamellar thickness and the side maximum.

7.3.2.1 Long-range order

Figure 7.4 shows an intensity profile of the 2D GISAXS images along q_z axis and its peak position fittings. The 2D GISAXS image was take ~ 9 min of vapor treatment in saturated CHXO atmosphere. The lamellar thickness deduced from the fittings ranged from 25.0 nm (close to the substrate - fitting shown in Figure 7.4b) to 26.1 nm (close to the surface - fitting shown in Figure 7.4a).

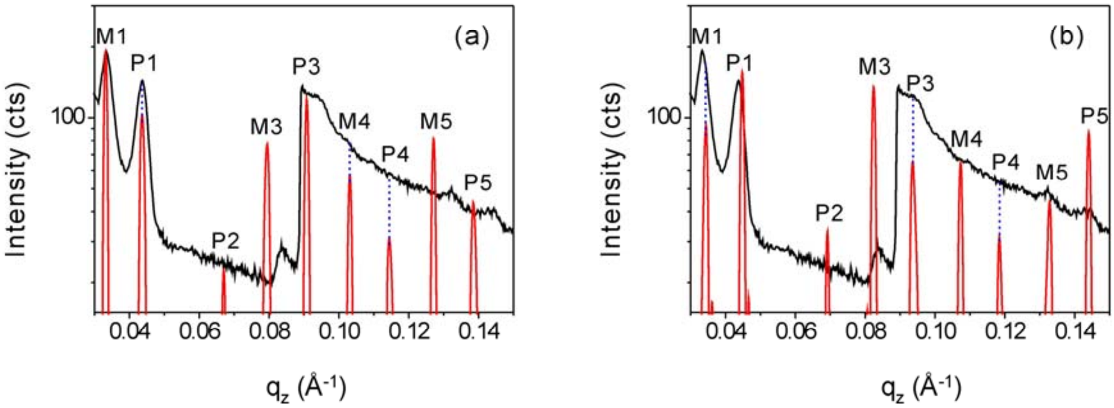

Figure 7.4 Intensity profile along q_z axis of a 2D GISAXS image together with its peak position fittings using *Layers*. The 2D GISAXS image was take after ~ 9 min of vapor treatment under saturated CHXO (measurement time 20 s). Since it is impossible to fit all the peak positions at the same time, only the 1st order peaks are chosen to fit in (a) and only the 5th order peaks are chosen to fit in (b). Two lamellar thicknesses of 26.1 nm and 25.0 nm are acquired respectively. The intensity increase at $q_z > 0.089$ Å^{-1} is due to the end of the rod-like beamstop.

Comparing Figure 7.4 to Figure 7.2, it is seen that: (i) The scattering intensities of DBS's after ~ 9 min of vapor treatment increased ~ 150% (also seen in Figure 7.5). (ii) The peak became sharper after vapor treatment (table 7-1) (iii) In the dry state, only the first 3 orders of DBS's appeared; However, after ~ 9 min of vapor treatment, even the 5th order DBS's appeared at $q_z = 0.133$ Å^{-1} and $q_z = 0.144$ Å^{-1}. Therefore, we conclude that, after 9 min of vapor treatment, the long-range order of the lamellae was improved.

Table 7-1 The FWHMs of the 1st order of the peaks from Figure 7.2 and 7.4

	M1 (Å^{-1})	P1 (Å^{-1})
Dry state	0.0032	0.0033
Swollen state	0.0029	0.0030

7.3.2.2 Lamellar thickness

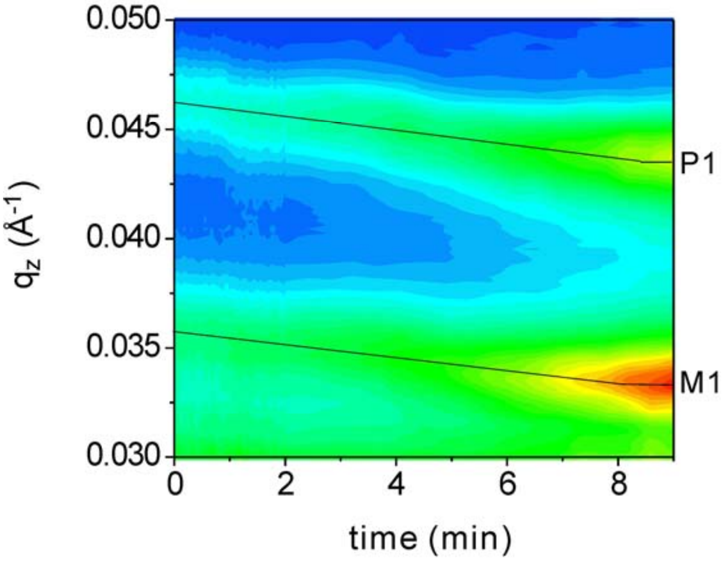

Figure 7.5 Map of the 1st order DBS's versus the vapor treatment time. The black line is the guider for the eyes. The linear intensity scale runs from 10 to 200 cts.

After the CHXO was injected to the sample cell, the DBS's shifted towards low-q_z continuously. A Map of the 1st order DBS's (M1, P1) versus the vapor treatment time is shown in Figure 7.5. The lamellar thicknesses were deduced from M1 and P1. The lamellae swelled from 22.2 nm in the dry state (fitting curve shown in Figure 7.2 a) to 26.1 nm in swollen state (fitting curve shown in Figure 7.4 a). The lamellar thickness leveled off after ~ 8 min and increased ~ 17%. Afterwards, side maximum was observed in much longer time scale and we will discuss it in the following section.

7.3.2.3 Side maximum

After ~ 12 min of vapor treatment, side maximums were seen in the DBS's and moving towards higher q_y with time (Figure 7.3). The side maximums indicate the formation of lateral structure. The length scale, D, of the lateral structure can be calculated using

$$D = \frac{2\pi}{q_y}$$

D decreased from ~209 nm and leveled off at 106 nm after ~ 80 min of vapor treatment as shown in Figure 7.6.

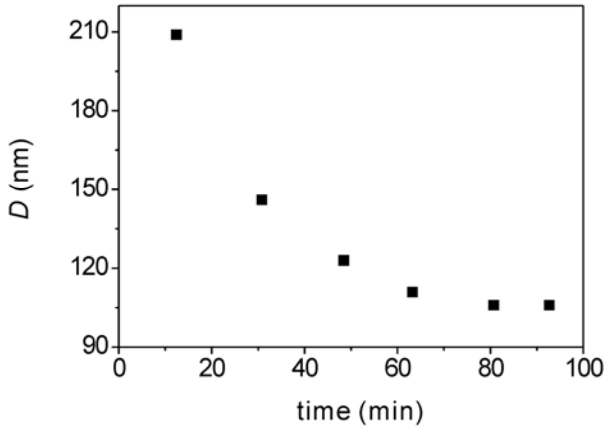

Figure 7.6 The lateral length scale *D* versus the vapor treatment time.

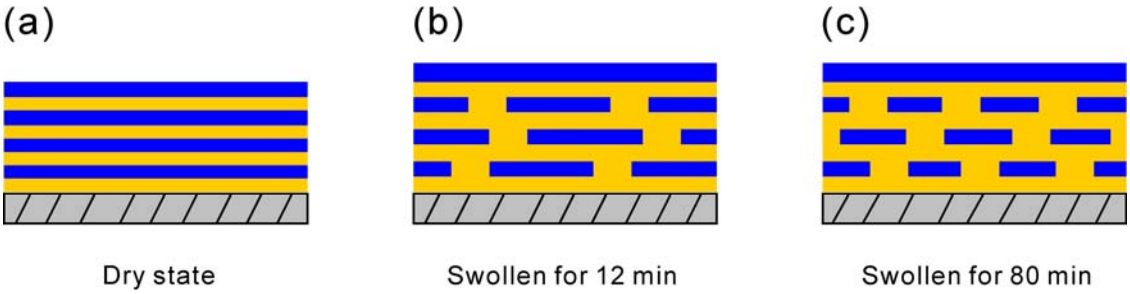

Figure 7.7 Schematics of the micro-phase transition. The yellow part represents the PS domain and the blue part represents the PB domain.

As seen in Figure 7.3, the side maximums are intensive and superposed on DBS's. it indicates that the lateral structure is very regular inside each layer. Together with the fact that CHXO is PS selective, we conclude that after ~ 12 min of vapor treatment in saturated CHXO atmosphere, regular holes (PS) were formed in the PB domains and the number of holes increased with time resulting a decrease of *D* (distance of neighbor holes) (Figure 7.6). Thus the lamellar micro-phase separation transformed to perforated layer micro-phase separation (Figure 7.7).

7.3.2.4 Elongation and bending of the DBS's

The DBS's were prolonged along q_y and bent towards the center of the specularly reflect beam (Figure 7.3). The similar phenomenon has been observed by us when the sample was treated in saturated toluene vapor [71]. We attribute it to the ripple formation. The ripple was formed probably because of the tension within each layer. In detail, the lamellae swelled instead of deswelling during solvent absorption due to the shielding effect of the existent lamellae (see §6.3.3.1). It led the polymer chains largely stretched and thus under tension.

7.3.2.5 Dewetting of the thin film

As can be seen from Figure 7.3 that: after ~ 60 min of vapor treatment, the intensity of the GISAXS image decreased again. We attribute it to the dewetting of the thin film. After 1 hour of vapor treatment, the thin film was damaged by dewetting which is seen by optical microscope images (Figure 7.8). Besides, even a direct look at the thin film by eyes, it was seen that the color of the film surface became darker.

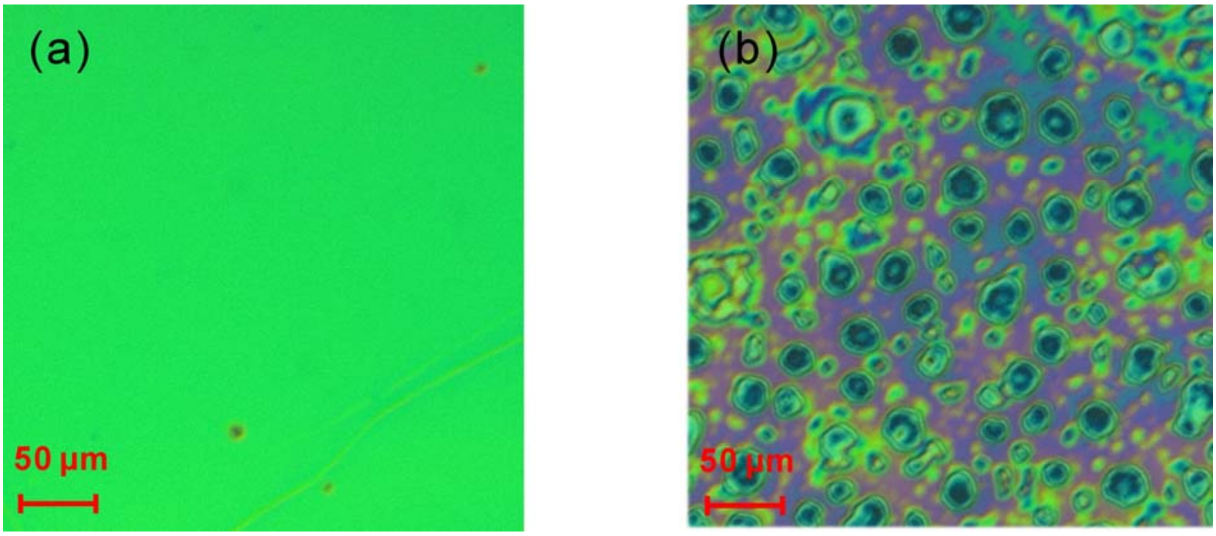

Figure 7.8 Optical microscope images of the thin film before vapor treatment (a) and after vapor treatment (b).

7.4 Conclusion

In this chapter, we report on the structural changes of thin film, which features initially fairly long-range order of lamellae with orientation parallel to the film surface, in the saturated CHXO atmosphere. Two processes, namely fast process and slow process, were observed by in-situ GISAXS measurement during this vapor treatment.

7.4.1 Fast process

The fast process took place roughly within the first 9 min. It is characterized by a strong increase of the scattering intensity, sharper DBS's and the appearance of 5^{th} order DBS's. All this observations point out that the long-range order of the lamellar micro-phase separation is further improved. We attribute the efficient improvement of the long-range order to the special properties of the CHXO, i.e. low T_g (162 K) and selective to the rigid PS domain. A detailed analysis of the position of the DBS's revealed that the lamellar thickness increased continuously with the increase of the film thickness. We have learned in previous chapters that the lamellar thickness should decrease with solvent absorption when the sample was in equilibrium. We attribute the increase of the lamellar thickness to the screening effect of the existent well-ordered lamellae (§6.3.3.1).

7.4.2 Slow process

After ~ 12 min of vapor treatment, regular holes were formed in the PB domain. The density of the holes increased with time. This can be seen from the decrease of the distance between neighbored holes. It revealed that the lamellar micro-phase separation has transformed to perforated layer micro-phase separation. Meanwhile, because of the tension in the thin film, ripple was formed and dewetting was observed.

Chapter 8

Summary

In this thesis, the focus is on the structural changes of lamellar P(S-*b*-B) thin films during vapor treatment. The effective Flory-Huggins segment-segment interaction parameter, χ_{eff} , the effective glass transition temperature, T_g and the volume fraction of one block, *f*, play an key role for the structural rearrangement. Furthermore, the existent structure also influences further structural changes.

The T_g of the PS domain is 76 °C which is higher than the room temperature. Thus in room temperature the polymer chains in the P(S-*b*-B) thin film are immobile and can not rearrange themselves to the micro-phase equilibration. However, when the solvent enters the sample the effective T_g of PS decreases. The effective T_g of PS can be deduced from the Kelley-Bueche equation (Equation 3.6). When the effective T_g of PS is lower than the ambient temperature, the sample becomes soft and the polymer chains become mobile. Thus it is possible for the sample to rearrange itself to the most favored state i.e. the micro-phase equilibrium. However, the micro-phase equilibrium is controlled by several parameters. Among them, χ and f are the most important two. Both of them are ϕ dependent. For nonselective (or close to nonselective) solvents, f is constant and $\chi_{eff} = \phi\chi$. Thus if too much solvent enters the polymer, resulting in $\chi_{eff} N < \left(\chi N\right)_{ODT}$, the equilibrium will be disordered state. Therefore, there is a window of ϕ which is suitable for vapor treatment.

During vapor treatment not only the long-range order but also the structure dimension is influenced by solvent uptake. In our case, D_{lam} is a function of ϕ . When the effective T_g of PS is still higher than ambient temperature, the polymer chains are immobile and they swell with the thin film, leading $D_{lam} \propto \phi^{-1}$. After enough solvent has entered the thin film and the effective T_g of PS is lower than ambient temperature, the polymer chains become mobile and can rearrange themselves to the equilibrium state. According to the mean-field theory, the $D_{lam} \propto \phi^{1/3}$. However, for the sample with initial long-range ordered parallel lamellae, $D_{lam} \propto \phi^{1/3}$, in many cases, is not fulfilled i.e. the D_{lam} could be larger than the mean-field prediction. We attribute it to the shielding effect of the existent lamellae. In detail, the decrease of D_{lam} i.e. more coiled chain conformation, requires larger cross-section for each chain. To make free space, part of the polymer chains has to be thrown out off the layer. The thrown out chains accumulate and form new lamellar layers. However, if the sample is in well-ordered lamellae, it is difficult to thrown out chains from one layer and even more difficult for those chains to travel cross other layers to accumulate and form new layers. Since the movement of polymer chains are largely shielded by existent lamellae, the D_{lam} can not decrease freely, thus a meta-stable state with larger D_{lam} was observed. Only when the D_{lam} is far away from the equilibrium value and the tension for coiling the chain is large enough, the meta-stable state will break. Subsequently, the rearrangement of the polymer chains in a large scale take place and new equilibration can establish.

Furthermore, the selectivity of the solvent plays an important role to the micro-phase separation morphology. When CHXO is used as solvent for vapor treatment, since the f_{PS} is then bigger than f_{PB}, after a prolonged treatment time, the lamellar micro-phase separation is transformed to perforated layer micro-phase separation.

Bibliography

1. Flory, P.J., *Thermodynamics of High Polymer Solutions.* Journal of Chemical Physics, 1941. **9**(8): p. 660.

2. Huggins, M.L., *Solutions of Long Chain Compounds.* Journal of Chemical Physics, 1941. **9**(5): p. 440.

3. Bates, F.S. and G.H. Fredrickson, *Block Copolymer Thermodynamics - Theory and Experiment.* Annual Review of Physical Chemistry, 1990. **41**: p. 525-557.

4. Hamley, I.W., *The physics of block copolymers*. Oxford science publications. 1998, Oxford ; New York: Oxford University Press. viii, 424 p.

5. Thurn-Albrecht, T., et al., *Ultrahigh-density nanowire arrays grown in self-assembled diblock copolymer templates.* Science, 2000. **290**(5499): p. 2126-2129.

6. Matsen, M. and M. Schick, *Stable and unstable phases of a diblock copolymer melt.* Physical Review Letters, 1994. **72**(16): p. 2660-2663.

7. Matsen, M. and F. Bates, *Unifying weak-and strong-segregation block copolymer theories.* Macromolecules, 1996. **29**(4): p. 1091-1098.

8. Urbas, A., Y. Fink, and E.L. Thomas, *One-dimensionally periodic dielectric reflectors from self-assembled block copolymer-homopolymer blends.* Macromolecules, 1999. **32**(14): p. 4748-4750.

9. Jin, C.Z., et al., *Synthesis, characterization and catalytic performance of Ti-containing mesoporous molecular sieves assembled from titanosilicate precursors.* Chemistry of Materials, 2007. **19**(7): p. 1664-1670.

10. Jung, Y.S., et al., *Nanowire Conductive Polymer Gas Sensor Patterned Using Self-Assembled Block Copolymer Lithography.* Nano Letters, 2008. **8**(11): p. 3776-3780.

11. de Boer, B., et al., *Supramolecular self-assembly and opto-electronic properties of semiconducting block copolymers.* Polymer, 2001. **42**(21): p. 9097-9109.

12. Albalak, R.J., E.L. Thomas, and M.S. Capel, *Thermal annealing of roll-cast triblock copolymer films.* Polymer, 1997. **38**(15): p. 3819-3825.

13. Elbs, H., et al., *Microdomain morphology of thin ABC triblock copolymer films.* Macromolecules, 1999. **32**(4): p. 1204-1211.

14. Xuan, Y., et al., *Morphology development of ultrathin symmetric diblock copolymer film via solvent vapor treatment.* Macromolecules, 2004. **37**(19): p. 7301-7307.

15. Peng, J., et al., *Morphologies in solvent-annealed thin films of symmetric diblock copolymer.* Journal of Chemical Physics, 2006. **125**(6): p. -.

16. Kim, S.H., et al., *Highly oriented and ordered arrays from block copolymers via solvent evaporation.* Advanced Materials, 2004. **16**(3): p. 226-231.

17. Kim, S.H., et al., *Salt complexation in block copolymer thin films.* Macromolecules, 2006. **39**(24): p. 8473-8479.

18. Fukunaga, K., et al., *Self-assembly of a lamellar ABC triblock copolymer thin film.* Macromolecules, 2002. **35**(11): p. 4406-4413.

19. Albalak, R.J., M.S. Capel, and E.L. Thomas, *Solvent swelling of roll-cast triblock copolymer films.* Polymer, 1998. **39**(8-9): p. 1647-1656.

20. Bates, F., *Polymer-polymer phase behavior.* Science, 1991. **251**(4996): p. 898.

21. Wasserman., E.H.a.R., *Microdomain structure and the interface in block copolymers.* In I. Goodman, editor, Developments in Block Copolymers, volume 1, chapter 4, pages 99-125. Applied Science Publishers, London, 1982.

22. Israelachvili, J., *Intermolecular and Structural Forces*. 1985, Academic Press, London.

23. Rubinstein, M. and R.H. Colby, *Polymer physics*. 2003, Oxford ; New York: Oxford University Press. xi, 440 p.

24. Price, C. and I. Goodman, *Developments in Block Copolymers.* London: Applied Science Publisher, 1982. **1**: p. 39-45.

25. Helfand, E., *Block copolymer theory. III. Statistical mechanics of the microdomain structure.* Macromolecules, 1975. **8**(4): p. 552-556.

26. Leibler, L., *Theory of Microphase Separation in Block Co-Polymers.* Macromolecules, 1980. **13**(6): p. 1602-1617.

27. De Gennes, P., *Theory of X-ray scattering by liquid macromolecules with heavy atom labels.* Journal de Physique, 1970. **31**(2-3): p. 235-238.

28. Helfand, E. and Y. Tagami, *Theory of Interface between Immiscible Polymers .2.* Journal of Chemical Physics, 1972. **56**(7): p. 3592-3601.

29. Banaszak, M. and M. Whitmore, *Self-consistent theory of block copolymer blends: Selective solvent.* Macromolecules, 1992. **25**(13): p. 3406-3412.

30. Lodge, T.P., et al., *Solvent distribution in weakly-ordered block copolymer solutions.* Macromolecules, 1997. **30**(20): p. 6139-6149.

31. Papadakis, C.M., et al., *A small-angle scattering study of the bulk structure of a symmetric diblock copolymer system.* Journal De Physique II, 1997. **7**(12): p. 1829-1854.

32. Jenckel, E. and R. Heusch, *Lowering the Freezing Temperature of Organic Glasses with Solvents.* Kolloid-Zeitschrift, 1953. **130**: p. 89-105.

33. Plazek, D., C. Seoul, and C. Bero, *Diluent Effects on Viscoelastic Behaviour.* Journal of Non-crystalline Solids, 1990. **131**(2): p. 570-578.

34. Kelley, F. and F. Bueche, *Viscosity and glass temperature relations for polymer-diluent systems.* Journal of Polymer Science, 1961. **50**(154): p. 549-556.

35. Braun, G. and A.J. Kovacs, in Proc. Int. Conf. on Phys. Non-Crystalline Solids, Delft, July, 1964, edited by J. A. Prins (North-Holland Pub. Co. Amsterdam, 1965).

36. Schuld, N. and B.A. Wolf, *Polymer-Solvent Interaction Parameters.* Polymer handbook, 1999.

37. Grulke, E., *Solubility parameter values.* Polymer handbook, 1999. **4**: p. 675-714.

38. Orwoll, R., *The polymer¨Csolvent interaction parameter x.* Rubber chemistry and technology, 1977. **50**: p. 451-79.

39. Barton, A.F.M., *CRC handbook of solubility parameters and other cohesion parameters*. 1983, Boca Raton, Fla.: CRC Press. 594 p.

40. Koningsveld, R. and L. Kleintjens, *Liquid-liquid phase separation in multicomponent polymer systems. X. Concentration dependence of the pair-interaction parameter in the system cyclohexane-polystyrene.* Macromolecules, 1971. **4**(5): p. 637-641.

41. Schuld, N. and B. Wolf, *Polymer-solvent interaction parameters.* Polymer Handbook, John Wiley & Sons, Inc, New York, 1999: p. 247-64.

42. Ndoni, S., et al., *Laboratory-Scale Setup for Anionic-Polymerization under Inert Atmosphere.* Review of Scientific Instruments, 1995. **66**(2): p. 1090-1095.

43. Papadakis, C.M., et al., *Identification of an intermediate-segregation regime in a diblock copolymer system.* Europhysics Letters, 1996. **36**(4): p. 289-294.

44. Hecht, E., *Optics.* 4th ed. Addison Wesley, 2002.

45. Holy, V., et al., *X-ray reflection from rough layered systems.* Physical review B, 1993. **47**(23): p. 15896-15903.

46. Als-Nielsen, J. and D. McMorrow, *Elements of modern X-ray physics*. 2001, New York: Wiley. xi, 318 p.

47. Parratt, L., *Surface studies of solids by total reflection of x-rays.* Physical Review, 1954. **95**(2): p. 359-369.

48. Vignaud, G., et al., *Analysis of X-ray reflectivity curves of non-Gaussian surfaces.* Thin Solid Films, 1998. **323**(1-2): p. 1-5.

49. Holý, V., U. Pietsch, and T. Baumbach, *High-resolution X-ray scattering from thin films and multilayers*. Springer tracts in modern physics,. 1999, Berlin ; New York: Springer. xi, 256 p.

50. Dubcek, P., et al., *GISAXS study of Cadmium Sulfide quantum dots GISAXS Sstudies of shape and size of CdS nanocrystals formed in monocrystalline Si by ion implantationobtained by ion implantation.* NUCLEAR INSTRUMENTS & METHODS IN PHYSICS RESEARCH SECTION B, 2003. **200**: p. 138-141.

51. Revenant, C., et al., *Quantitative analysis of grazing incidence small-angle x-ray scattering: Pd/MgO (001) growth.* Physical review B, 2004. **69**(3): p. 35411.

52. Glatter, O. and O. Kratky, *Small angle X-ray scattering*. 1982: Academic Press London.

53. Metzger, T., et al., *Shape, size, strain and correlations in quantum dot systems studied by grazing incidence X-ray scattering methods.* Thin Solid Films, 1998. **336**(1-2): p. 1-8.

54. Renaud, G., et al., *Real-time monitoring of growing nanoparticles.* Science, 2003. **300**(5624): p. 1416.

55. Smilgies, D.-M., et al., *Characterization of Polymer Thin Films with Small-Angle X-ray Scattering under Grazing Incidence (GISAXS).* Synchrotron Radiation News, 2002. **15**(No.5): p. 35-42.

56. Gibaud, A., et al., *Evaporation-controlled self-assembly of silica surfactant mesophases.* J. Phys. Chem. B, 2003. **107**(25): p. 6114-6118.

57. Saunders, A., et al., *Columnar self-assembly of colloidal nanodisks.* Nano Lett, 2006. **6**(12): p. 2959-2963.

58. Sinha, S., et al., *X-ray and neutron scattering from rough surfaces.* Physical review B, 1988. **38**(4): p. 2297-2311.

59. Rauscher, M., T. Salditt, and H. Spohn, *Small-angle x-ray scattering under grazing incidence: The cross section in the distorted-wave Born approximation.* Physical review B, 1995. **52**(23): p. 16855-16863.

60. Lazzari, R., *IsGISAXS: a program for grazing-incidence small-angle X-ray scattering analysis of supported islands.* Journal of Applied Crystallography, 2002. **35**: p. 406-421.

61. From home page of Prof. Papadakis, C.M., http://www.e13.physik.tu-muenchen.de/structpol/index.en.php.

62. Roth, S., et al., *Small-angle options of the upgraded ultrasmall-angle x-ray scattering beamline BW4 at HASYLAB.* Review of Scientific Instruments, 2006. **77**: p. 085106.

63. Busch, P., et al., *Grazing-incidence small-angle X-ray scattering from thin polymer films with lamellar structures-the scattering cross section in the distorted-wave Born approximation.* Journal of Applied Crystallography, 2006. **39**: p. 433-442.

64. Layer, *Written by Markus Rauscher.* Max-Planck-Institute for Metals research, Stuttgart, Germany.

65. Busch, P., et al., *Inner structure of thin films of lamellar poly(styrene-b-butadiene) diblock copolymers as revealed by grazing-incidence small-angle scattering.* Macromolecules, 2007. **40**(3): p. 630-640.

66. Dosch, H., B. Batterman, and D. Wack, *Depth-controlled grazing-incidence diffraction of synchrotron x radiation.* Physical review letters, 1986. **56**(11): p. 1144-1147.

67. Busch, P., et al., *Lamellar diblock copolymer thin films investigated by tapping mode atomic force microscopy: Molar-mass dependence of surface ordering.* Macromolecules, 2003. **36**(23): p. 8717-8727.

68. Tolan, M., *X-ray scattering from soft-matter thin films : materials science and basic research*. Springer tracts in modern physics ;. 1999, Berlin ; New York: Springer. viii, 197 p.

69. Krigbaum, W.R. and D.O. Geymer, *Thermodynamics of Polymer Solutions - the Polystyrene Cyclohexane System near the Flory Theta-Temperature.* Journal of the American Chemical Society, 1959. **81**(8): p. 1859-1868.

70. Brandrup, J., E.H. Immergut, and E.A. Grulke, *Polymer Handbook.* 4th ed. 1999, New York: Wiley.

71. Papadakis, C.M., et al., *Structural Instabilities in Lamellar Diblock Copolymer Thin Films During Solvent Vapor Uptake.* Langmuir, 2008. **24**(24): p. 13815-13818.

72. Shibayama, M., et al., *Ordered Structure in Block Polymer-Solutions .3. Concentration-Dependence of Microdomains in Non-Selective Solvents.* Macromolecules, 1983. **16**(9): p. 1427-1433.

73. Marcus, Y., *The properties of solvents*. Wiley series in solution chemistry. 1998, Chichester ; New York: Wiley. xiv, 239 p.

74. Prevosto, D., et al., *Secondary dielectric relaxation in decahydroisoquinoline-cyclohexane mixture.* Journal of Non-Crystalline Solids, 2006. **352**(42-49): p. 4685-4689.

75. Helfand, E. and Y. Tagami, *Theory of Interface between Immiscible Polymers .2.* Journal of Chemical Physics, 1972. **56**(7): p. 3592-3601.

76. Fredrickson, G.H. and E. Helfand, *Fluctuation Effects in the Theory of Microphase Separation in Block Copolymers.* Journal of Chemical Physics, 1987. **87**(1): p. 697-705.

77. Noolandi, J. and K.M. Hong, *Theory of Inhomogeneous Polymers in Presence of Solvent.* Ferroelectrics, 1980. **30**(1-4): p. 117-123.

78. Lee, B., et al., *Structural analysis of block copolymer thin films with grazing incidence small-angle X-ray scattering.* Macromolecules, 2005. **38**(10): p. 4311-4323.

Acknowledgement

I would like to express my deepest gratitude and appreciation to my supervisor Prof. Dr. Christine M. Papadakis. She has led me into the fascinating research field of block copolymers. I would not be able to finish this thesis without her patient guidance and many useful discussions. Her valuable insight and continuous support both within and beyond this thesis work always encourages me and helps me to reach my goals

I thank Prof. Dr. Peter Müller-Buschbaum, acting chair person of the Physik Department E13, for his help, insight and advice.

I thank Prof. Katharina Krischer, my co-advisor, for valuable discussion and widening of my knowledge.

My special thanks to Prof. Dorthe Posselt at IMFUFA, the Department of Science, Systems and Models, Roskilde University, Denmark for her assistance, cooperation and fruitful discussions during GISASX experiment.

I wish to acknowledge Dr. Detlef-M. Smilgies at the Cornell High Energy Synchrotron Source (CHESS), Cornell University, Ithaca, New York and Dr. Stephan V. Roth at the Hamburger Synchrotronstrahlungslabor (HASYLAB) for their enormous help, assistance and fruitful discussions during the GISAXS experiments.

Many thanks go to all past and present E13 group members especially Dr. Peter Busch, Dr. Charles Darko, Dr. Jan Perlich, Josseph Adelsberger, Alessandro Sepe, Tilo Hoppe, Dr. Ezzeldin Metwalli Ali, Weinan Wang for their help and kindness.

I acknowledge to the Bavarian State Ministry of Sciences, Research and the Arts for financial support through the International Graduate School “Materials Science of Complex Interfaces (CompInt)”.